

Symmetry Origin and Microscopic Mechanism of Electrical Magnetochiral Anisotropy in Tellurium

Manuel Suárez-Rodríguez¹, Beatriz Martín-García^{1,2}, Francesco Calavalle¹, Stepan S. Tsirkin^{2,3}, Ivo Souza^{2,3}, Fernando De Juan^{2,4}, Albert Fert^{4,5,6}, Marco Gobbi^{2,3,*}, Luis E. Hueso^{1,2,†}, and Fèlix Casanova^{1,2,‡}.

¹*CIC nanoGUNE BRTA, 20018 Donostia-San Sebastián, Basque Country, Spain*

²*IKERBASQUE, Basque Foundation for Science, 48009 Bilbao, Basque Country, Spain*

³*Centro de Física de Materiales CSIC-UPV/EHU, 20018 Donostia-San Sebastián, Basque Country, Spain*

⁴*Donostia International Physics Center, 20018 Donostia-San Sebastián, Basque Country, Spain*

⁵*Laboratoire Albert Fert, CNRS, Thales, Université Paris-Saclay, 91767 Palaiseau, France*

⁶*Department of Materials Physics UPV/EHU, 20018 Donostia-San Sebastián, Basque Country, Spain*

Correspondence to: *marco.gobbi@ehu.eus; †l.hueso@nanogune.eu; ‡f.casanova@nanogune.eu

Abstract.-Non-linear transport effects in response to external magnetic fields, i.e. electrical magnetochiral anisotropy (eMChA), have attracted much attention for their importance to study quantum and spin-related phenomena. Indeed, they have permitted the exploration of topological surface states and charge-to-spin conversion processes in low-symmetry systems. Nevertheless, despite the inherent correlation between the symmetry of the material under examination and its non-linear transport characteristics, there is a lack of experimental demonstration to delve into this relationship and to unveil their microscopic mechanisms. Here, we study eMChA in chiral elemental Tellurium (Te) along different crystallographic directions, establishing the connection between the different eMChA components and the crystal symmetry of Te. We observed different longitudinal eMChA components with collinear current and magnetic field, demonstrating experimentally the radial angular momentum texture of Te. We also measured a transverse non-linear resistance which, as the longitudinal counterpart, scales bilinearly with current and magnetic fields, illustrating that they are different manifestations of the same effect. Finally, we study the scaling law of the eMChA, evidencing that extrinsic scattering from dynamic sources is the dominant microscopic mechanism. These findings underscore the efficacy of symmetry-based investigations in understanding and predicting non-linear transport phenomena, with potential applications in spintronics and energy harvesting.

Introduction.-Low-symmetry materials have revolutionized the field of electronic transport. This disruption stems from the breaking of inversion symmetry within such systems, which permits non-linear transport effects where the voltage (V) scales quadratically with the current (I) [1]. Notably, this non-linear behavior can manifest both with and without the presence of external magnetic fields (B) [2].

On the one hand, non-linear transport effects in the absence of external magnetic fields ($I \propto V^2$) have recently attracted much attention [3-6]. Indeed, they allowed for the study of novel quantum properties, such as the Berry curvature [7,8] or quantum metric [9,10], and have the potential to be exploited for energy harvesting through radiofrequency rectification [11-14]. Systematic studies have been performed, identifying both longitudinal (i.e., non-linear conductivity [15,16]) and transverse (i.e., non-linear Hall effect (NLHE) [3,4,17]) components, and its connection with the crystal symmetry of the tested material.

On the other hand, non-linear transport effects in the presence of external magnetic fields ($I \propto V^2 B$) have great importance for spintronics as they can be employed for the investigation of spin-related effects [18]. In general, these phenomena are named electrical magnetochiral anisotropy (eMChA) [19,20]. However, as most reports are focused on the longitudinal manifestation, they are commonly known as unidirectional magnetoresistance (UMR) [18] or bilinear magnetoresistance (BMR) [21,22]. Although there are few reports on the transverse manifestation, i.e., non-linear planar Hall effect (NLPHE) [23,24], an experimental demonstration of the fundamental connection between the two effects and the crystal symmetry of the material is still absent. Furthermore, the microscopic mechanisms behind these effects remain unexplored. Chiral materials provide an exceptional platform for investigating non-linear transport effects due to their absence of both inversion and mirror symmetry [25,26]. In this context, a material with strong spin-orbit coupling such as chiral tellurium (Te) [27], which can be chemically synthesized [28] and patterned into desired shapes, emerges as the ideal candidate.

In this letter, we present an experimental study of eMChA in Te, encompassing both longitudinal and transverse measurements, along with an analysis of the crystallographic direction dependence. Te flakes are grown via a hydrothermal process and patterned into star-shaped structures, enabling precise measurements along different crystallographic directions. By taking into account the symmetry of trigonal Te, we derive equations that accurately describe the experimental non-linear transport in Te across all configurations. We observe a longitudinal eMChA, i.e. UMR or BMR, when B and I are aligned along the z -axis, consistently with previous reports [18]. Remarkably, we also observe a longitudinal eMChA when both B and I are along the x -axis, thus demonstrating the anisotropic radial angular momentum texture of Te by electrical means. Additionally, we detect a transverse eMChA, i.e., NLPHE, when B is along the z -axis and I is along the x -axis. We illustrate that this transverse non-linear resistance exhibits bilinear dependence on B and I . Finally, by examining the dependence of the eMChA on the resistivity, we establish that the eMChA in Te is primarily governed by extrinsic mechanisms. Our findings underscore how the analysis of crystal symmetry and resistivity scaling facilitate the prediction of non-linear transport effects, providing insights into permitted components and microscopic mechanisms. Therefore, we aim to inspire similar analyses devoted to discovering novel systems suitable for spintronics and energy harvesting applications.

Anisotropic transport.-Trigonal elemental Te displays a chiral crystal structure, belonging to $P3_121$ (right-handed) or $P3_221$ (left-handed) space groups. It is composed of covalently bonded Te helices along the z -axis [Fig. 1(a)], stacked together by van der Waals interactions. The projection of the Te helices in the xy plane shows an atomic triangle pattern [Fig. 1(b)]. We grow single crystalline Te flakes following a hydrothermal process [28], and we pattern them into a star-shaped device by e-beam lithography and reactive ion etching. Finally, we contact them with Pt electrodes allowing electrical measurements for different crystallographic directions (for more details, see Supplementary Section 1). A harmonic current at frequency $\omega = 31$ Hz (I^ω) is injected between two electrodes aligned in the same direction at an angle θ from the chiral z -axis. During this process, both the first- (V^ω) and second- ($V^{2\omega}$) harmonic voltages are recorded. The measurements are conducted in both longitudinal (V_\parallel) and transverse (V_\perp) configurations using a rotating reference frame. Our setup also enables temperature modulation (2-300 K) and the

application of magnetic fields up to 9 T in all directions [Fig. 1(c)].

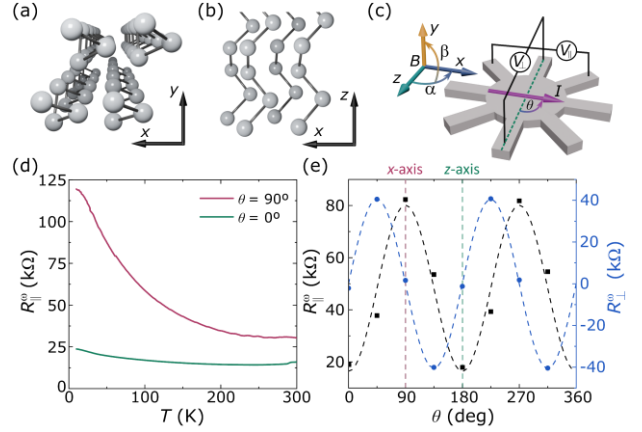


FIG 1. Anisotropic transport in Te. (a), (b) Crystal structure sketch of trigonal Te in the (a) $x - y$ plane and (b) $x - z$ plane. (c) Sketch of the star-shaped Te device. An oscillating current at frequency ω (I^ω) is injected at an angle θ with respect to the chiral z -axis, and both longitudinal (V_\parallel) and transverse (V_\perp) voltages are recorded. The relative orientation between an external magnetic field and the device is also indicated. (d) Temperature dependence of the first-harmonic longitudinal resistance (R_\parallel^ω) when I^ω is injected along x - ($\theta = 90^\circ$) and z -axis ($\theta = 0^\circ$). (e) First-harmonic longitudinal (R_\parallel^ω) and transverse (R_\perp^ω) resistance as a function of θ at 50 K. The dashed lines are fits to the equations introduced in the main text. The R_\parallel^ω and R_\perp^ω values are obtained from the linear fittings in Fig. S1. All measurements were performed at $B = 0$ T with $|I^\omega| = 1$ μ A.

Figure 1(d) shows the temperature dependence of the first-harmonic longitudinal resistance ($R_\parallel^\omega \equiv \frac{V_\parallel^\omega}{I^\omega}$) along the z -axis ($\theta = 0^\circ$) as well as the x -axis ($\theta = 90^\circ$). We note that the resistance along the x -axis is much higher than along the z -axis, which is a direct consequence of the anisotropic crystal structure: the electronic transport is much more favorable along the covalently-bonded Te helices (z -axis) than between them (x -axis). To further study the anisotropic electronic transport in Te and to ensure a proper control of current directionality, we measure the first-harmonic longitudinal (R_\parallel^ω) and transverse resistance ($R_\perp^\omega \equiv \frac{V_\perp^\omega}{I^\omega}$) for different θ angles, between the current I^ω and the chiral z -axis [Fig. 1(e)]. On the one hand, R_\parallel^ω follows $R_\parallel^\omega(\theta) = (L_\parallel/A)[\rho_{zz}\cos^2(\theta) + \rho_{xx}\sin^2(\theta)]$, where L_\parallel is the distance between longitudinal contacts, A is the cross section of the contacts, and ρ_{zz} and ρ_{xx} are the resistivities along the z - and x -axis, respectively. We observe that $\rho_{xx} \gg \rho_{zz}$, in agreement with the temperature dependence study [Fig. 1(d)]. On the other hand, R_\perp^ω follows $R_\perp^\omega(\theta) = (L_\perp/A)(\rho_{xx} - \rho_{zz})\cos(\theta)\sin(\theta)$, where L_\perp is the distance between

transverse contacts. The excellent fittings of the experimental data to the expected θ dependence indicate a precise control of the current directionality in our star-shaped Te devices, allowing for further crystallographic dependent transport experiments (for more details, see Supplementary Section 2).

Anisotropic magnetotransport.—Recently, the electronic transport properties of Te in response to an external magnetic field have attracted much attention. Negative magnetoresistance [18] [29] and planar Hall effect [30] have been reported, both being considered as possible signatures of Weyl physics [30]. However, it is worth noting that the Weyl points in trigonal Te are at ~ 0.4 and 0.5 eV below the top of the valence band [31], thus far away from where the electronic transport generally occurs [32]. In the following, we will demonstrate that, from crystal symmetry considerations, it is possible to analyze the different magnetoresistance and Hall components in trigonal Te.

The first-order electric field (E_i^ω) in response to a current density (j_j^ω) and a magnetic field ($B_{k,l}$) can be expressed through the material Magnetoresistance (T_{ijkl}) and Hall (R_{ijk}) tensors as $E_i^\omega = T_{ijkl}j_j^\omega B_k B_l + R_{ijk}j_j^\omega B_k$. We observe that the magnetoresistance and Hall contributions are even and odd, respectively, with respect to the magnetic field. Therefore, it is possible to differentiate them experimentally. For Te with $P3_121$ or $P3_221$ space group symmetry, considering electric fields and currents in the $x-z$ plane and magnetic fields in all directions, the Magnetoresistance and Hall tensors have 9 and 2 non-zero elements, respectively [33]:

$$T_{ijkl}^{Te} = \begin{pmatrix} T_{xxxx} & T_{xxyy} & T_{xxzz} & T_{xxyz} & 0 & 0 \\ T_{zzxx} & T_{zzyy} & T_{zzzz} & 0 & 0 & 0 \\ 0 & 0 & 0 & 0 & T_{xzzx} & T_{zxxy} \end{pmatrix} \quad (1)$$

$$R_{ijk}^{Te} = \begin{pmatrix} 0 & 0 & 0 \\ 0 & R_{xzy} & 0 \\ 0 & -R_{xzy} & 0 \\ 0 & 0 & 0 \end{pmatrix} \quad (2)$$

Therefore, we can directly obtain the expressions of the longitudinal and transverse electric fields as a function of θ , α , and β angles in terms of T_{ijkl} and R_{ijk} (see Supplementary Section 2). In order to disentangle the different components, we have measured the Te magnetoresistance ($MR \equiv \frac{R_{\parallel}^\omega(B=9T) - R_{\parallel}^\omega(B=0T)}{R_{\parallel}^\omega(B=0T)}$) for $\theta = 0^\circ$ [Fig. 2(a)] and $\theta = 90^\circ$ [Fig. 2(b)], and also the first-harmonic transverse resistance (R_{\perp}^ω) for $\theta = 0^\circ$ [Fig. 2(c)] and $\theta = 90^\circ$ [Fig. 2(d)], by rotating a magnetic field $B = 9$ T in both α - and β - planes [Fig. 1(c)].

Figures 2(a) and 2(b) manifest that the equations obtained from our analysis based on Te crystal symmetry perfectly capture the experimental response, both for the α -angle dependence (blue curves), $MR = (B^2/\rho_{zz})\cos^2(\theta)[T_{zzxx}\sin^2(\alpha) + T_{zzzz}\cos^2(\alpha)] + (B^2/\rho_{xx})\sin^2(\theta)[T_{xxxx}\sin^2(\alpha) + T_{xxzz}\cos^2(\alpha)]$ and for the β -angle dependence (red curves), $MR = (B^2/\rho_{zz})\cos^2(\theta)[T_{zzyy}\sin^2(\beta) + T_{zzzz}\cos^2(\beta)] + (B^2/\rho_{xx})\sin^2(\theta)[T_{xxyy}\sin(\beta)\cos(\beta) + T_{xxyy}\sin^2(\beta) + T_{xxzz}\cos^2(\beta)]$ (for more details, see Supplementary Section 2). Importantly, we recognized that the critical parameter for the first-order magnetoresistance response is the direction of the magnetic field. The MR is negative when B is along the z -axis ($\alpha = \beta = 0^\circ$), independently on the direction of the current [see also Figs. S2(a),(b)]. Previous reports have studied the magnetotransport of Te only when the current is along the z -axis, and related its negative MR with the chiral anomaly [30]. However, the chiral anomaly can only apply for $B \parallel I^\omega$ [34], and we also observe negative MR when $B \perp I^\omega$. Therefore, our observation suggests a different mechanism behind the negative MR in Te, such as Berry curvature or orbital moments [35-38]. A temperature dependence of the MR can be found in Figs. S2(c),(d).

Regarding the transverse measurements [Figs. 2(c),(d)], we observe that the β -angle dependence (red curves) is given by the Hall component $R_{\perp}^\omega = (L_{\parallel}/A)R_{xzy}B\sin(\beta)[\sin^2(\theta) + \cos^2(\theta)]$. Indeed, when the magnetic field is out-of-plane ($B \parallel y$ -axis) we detect the ordinary Hall effect in Te, whose sign and magnitude indicate that the electronic transport is dominated by holes and permits to obtain the carrier density $n_h \approx 6.5 \times 10^{17} \text{ cm}^{-3}$ [Figs. S2(e),(f)]. For the α -angle dependence (blue curves), we observe the so-called planar Hall effect. However, as we can extract from our equations, $R_{\perp}^\omega = 2(L_{\perp}/A)T_{xzzx}B^2\sin(\alpha)\sin(\beta)[\sin^2(\theta) - \cos^2(\theta)]$, the planar Hall effect is even respect to B , thus not being a true Hall effect [39]. The planar Hall effect has been considered a signature of Weyl physics [30], but we demonstrate that it is directly allowed by the symmetry of Te and its associated MR tensor (T_{xzzx} component). Therefore, as for the negative MR, its origin may be related to Berry curvature or orbital moments. More importantly, the equations obtained from the analysis of Te symmetry perfectly capture all the experimental observations (solid lines in Fig. 2), demonstrating to be a powerful method. From the fittings of the experimental data, we determined the values of the resistivity, magnetoresistance, and Hall tensors components (Table S1).

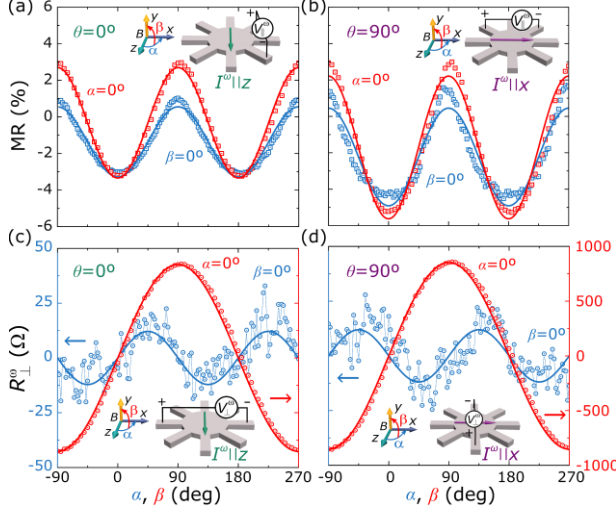


FIG 2. Anisotropic magnetotransport in Te. (a), (b) Te Magnetoresistance $[MR \equiv (R_{\parallel}^{\omega}(B = 9T) - R_{\parallel}^{\omega}(B = 0T))/R_{\parallel}^{\omega}(B = 0T)]$ as a function of α -angle ($\beta=0^{\circ}$, blue curve) and β -angle ($\alpha=0^{\circ}$, red curve) when the current is along (a) z -axis ($\theta = 0^{\circ}$) and (b) x -axis ($\theta = 90^{\circ}$). (c),(d) First-harmonic transverse resistance (R_{\perp}^{ω}) as a function of α -angle ($\beta=0^{\circ}$, blue curve) and β -angle ($\alpha=0^{\circ}$, red curve) when current is along (c) z -axis ($\theta = 0^{\circ}$) and (d) x -axis ($\theta = 90^{\circ}$). All measurements were performed at 50 K and $B = 9$ T. The solid lines are fits to the equations introduced in the main text.

Electrical magnetochiral anisotropy.-Non-linear transport effects in response to external magnetic fields, i.e. eMChA, have attracted much attention for their importance on spintronics. Indeed, eMChA has been reported in two-dimensional electron gases [22] and topological insulators [21], unveiling the helical spin texture of these systems. Recently, eMChA has also been reported in elemental Te [18]. The particular symmetry of chiral Te gives rise to an anisotropic handedness-dependent radial spin texture [27], which is compatible with the eMChA experiments. Therefore, the eMChA measurements can be exploited to determine the handedness of Te crystals [18]. These experiments have been limited to currents along the chiral z -axis. However, the Te chiral structure offers a rich family of eMChA components [20] that can be investigated with our star-shaped Te devices.

In general, the second-order current density ($j_i^{2\omega}$) in response to an electric ($E_{j,k}^{\omega}$) and magnetic (B_l) field can be expressed through the eMChA conductivity tensor (σ_{ijkl}) of the material as $j_i^{2\omega} = \sigma_{ijkl} E_j^{\omega} E_k^{\omega} B_l$. For Te with $P3_121$ or $P3_221$ space group symmetries, considering electric fields and currents in the $x-z$ plane and magnetic fields in all directions, the eMChA

conductivity tensor has 8 independent non-zero elements [33]:

$$\sigma_{ijkl} = \begin{pmatrix} \sigma_{xxxx} & \sigma_{zzzz} & 0 \\ 0 & 0 & \sigma_{xxzy} \\ 0 & 0 & \sigma_{xxzz} \\ 0 & 0 & \sigma_{zxxz} \\ 0 & \sigma_{zxxz} & 0 \\ \sigma_{zxxz} & \sigma_{zzzz} & 0 \end{pmatrix} \quad (3)$$

As in the previous section, we can measure both the longitudinal and transverse response when the current is along z -axis ($\theta = 0^{\circ}$) and x -axis ($\theta = 90^{\circ}$). For such current directions, the longitudinal second-harmonic voltage ($V_{\parallel}^{2\omega}$) is given by (for more details, see Supplementary Section 3):

$$\theta = 0^{\circ} \rightarrow V_{\parallel}^{2\omega} = -\frac{L_{\parallel}}{A^2} (I^{\omega})^2 R_{zz}^3 \sigma_{zzzz} B \cos(\alpha) \cos(\beta) \quad (4)$$

$$\theta = 90^{\circ} \rightarrow V_{\parallel}^{2\omega} = -\frac{L_{\parallel}}{A^2} (I^{\omega})^2 R_{xx}^3 \sigma_{xxxx} B \sin(\alpha) \cos(\beta) \quad (5)$$

To explore the longitudinal components, we recorded $V_{\parallel}^{2\omega}$ as a function of the α -angle at $B = 9$ T and $\beta = 0^{\circ}$ [Fig. 3(a)]. For $I^{\omega} \parallel z$ -axis ($\theta = 0^{\circ}$), the maximum signal is when B and I^{ω} are collinear ($B \parallel I^{\omega} \parallel z$), as indicated by Eq. (4) and in agreement with previous reports [18]. Interestingly, for $I^{\omega} \parallel x$ -axis ($\theta = 90^{\circ}$), the maximum signal is also when B and I^{ω} are collinear ($B \parallel I^{\omega} \parallel x$), as predicted by Eq. (5). Therefore, these results demonstrate the radial angular momentum texture of Te by purely electrical means. The eMChA is maximum when the external magnetic field is parallel to the current-induced angular momentum accumulation (J_i), which points along the z -axis when the current is along the z -axis ($J_z \parallel I^{\omega} \parallel z$), and points along the x -axis when the current is along the x -axis ($J_x \parallel I^{\omega} \parallel x$) [21]. The longitudinal eMChA is usually related to the spin texture of the system [21] [22]. However, recent theoretical works suggest that the orbital contribution may be dominant [40]. Indeed, theoretical predictions indicate that in Te, the orbital (L_i) is stronger than the spin component (S_i) and, thus, dictates the eMChA response [20,41]. Therefore, as they have the same symmetry and we cannot distinguish between them in our experiments, we have decided to use the term "angular momentum texture" to account for both contributions ($J_i = L_i + S_i$). From the fittings, we obtain the values of $\sigma_{xxxx} = (-5.31 \pm 0.48) 10^{-6} \text{ AV}^{-2}\text{T}$ and $\sigma_{zzzz} = (-1.283 \pm 0.048) 10^{-4} \text{ AV}^{-2}\text{T}$. The substantial difference between the magnitudes of σ_{xxxx} and σ_{zzzz} indicates that the angular momentum texture of Te is not merely radial but also anisotropic.

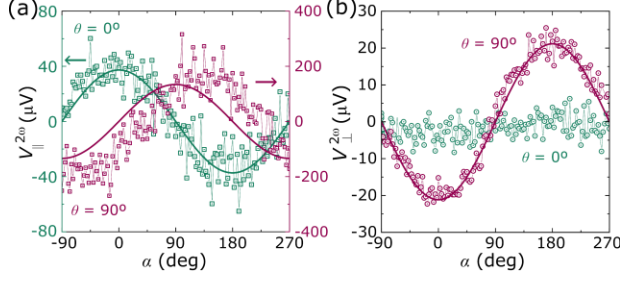


FIG 3. Crystallographic direction-dependence of eMChA in Te. Second-harmonic (a) longitudinal ($V_{\parallel}^{2\omega}$) and (b) transverse ($V_{\perp}^{2\omega}$) voltage when current is along the z -axis ($\theta = 0^\circ$) and the x -axis ($\theta = 90^\circ$) as a function of α -angle at 9 T and $\beta = 0^\circ$. All measurements were performed at 50 K with $|I^\omega| = 1 \mu\text{A}$. The solid lines are fits of the experimental data to Eqs. (4-7).

The transverse eMChA, i.e. NLPHE, has been much less studied in literature [23,24]. Indeed, current direction-dependent studies, which identify the connections between the eMChA components and the crystal symmetry of the studied material, are still missing. Here, we employ our analysis based on Te symmetry, which determines that the transverse second-harmonic voltage ($V_{\perp}^{2\omega}$) is given by (for more details, see Supplementary Section 3):

$$\theta = 0^\circ \rightarrow V_{\perp}^{2\omega} = -\frac{L_{\perp}}{A^2} (I^\omega)^2 \rho_{xx} \rho_{zz}^2 \sigma_{xzzx} B \sin(\alpha) \cos(\beta) \quad (6)$$

$$\theta = 90^\circ \rightarrow V_{\perp}^{2\omega} = -\frac{L_{\perp}}{A^2} (I^\omega)^2 \rho_{xx}^2 \rho_{zz} B [\sigma_{zxxz} \cos(\alpha) \cos(\beta) + \sigma_{zxy} \sin(\beta)] \quad (7)$$

Hence, to explore the transverse components, we record $V_{\perp}^{2\omega}$ as a function of the α -angle at $B = 9$ T [Fig. 3(b)]. We note that, in the α -angle dependence at $\beta = 0^\circ$, the component σ_{zxy} does not contribute [see Eq. (7)]. Remarkably, we observe a clear eMChA signal when $I^\omega \parallel x$ (magenta curve, $\theta = 90^\circ$) but not when $I^\omega \parallel z$ (green curve, $\theta = 0^\circ$). Assuming σ_{zxxz} and σ_{xzzx} to be of the same order of magnitude, $V_{\perp}^{2\omega}$ is expected to be larger for $I^\omega \parallel x$, because $\rho_{xx} \gg \rho_{zz}$ [see equations (6) and (7)]. Moreover, $V_{\perp}^{2\omega}$ in response to I^ω and B has also a contribution coming from a combination of non-linear conductivity and ordinary Hall. For $\beta = 0^\circ$, this extra contribution has no impact when $I^\omega \parallel x$ but does have one when $I^\omega \parallel z$, and, therefore, it may cancel out the eMChA component (for more details, see Supplementary Section 4). From the fitting to Eq. (7), we quantify the value of $\sigma_{zxxz} = (2.603 \pm 0.039) 10^{-6} \text{AV}^{-2}\text{T}$. More importantly, for both longitudinal and transverse measurements, our symmetry analysis perfectly capture the experimental response (solid lines in Fig. 3), unveiling the relationships between voltage, current and magnetic field directions for which the eMChA in Te is allowed.

We further explore the transverse eMChA, by studying its current-, field-, and temperature-dependence. The longitudinal eMChA, when defined as a resistance ($R_{\parallel}^{2\omega} = V_{\parallel}^{2\omega}/I^\omega$), is commonly known as BMR because it depends linearly on current and magnetic field (Eqs. 4-5). However, as dictated by Eqs. (6-7), the transverse non-linear resistance ($R_{\perp}^{2\omega} = V_{\perp}^{2\omega}/I^\omega$) is also expected to depend linearly on both. To prove this, we record $V_{\perp}^{2\omega}$ for different currents at $\theta = 90^\circ$ and $B = 9$ T [Fig. 4(a)] and for different magnetic fields at $|I^\omega| = 1 \mu\text{A}$ [Fig. 4(b)], as a function of β -angle at $\alpha = 0^\circ$. We note that, to fully demonstrate the accuracy of our symmetry analysis, we have studied $V_{\perp}^{2\omega}$ as a function of α -angle in Fig. 3 and as a function of β -angle in Fig. 4. As observed, the experimental behavior of $V_{\perp}^{2\omega}$ is perfectly captured by Eq. (7), and $R_{\perp}^{2\omega}$ depends bilinearly on current and magnetic field [insets in Fig. 4(a),(b)]. The same bilinear dependence is obtained with the results as a function of α -angle (Fig. S3), providing further evidence of the accuracy of our symmetry analysis. Eq. (7) includes a term $\sigma_{zxy} \sin(\beta)$, but experimentally no $\sin(\beta)$ dependence is observed. The reason may be that σ_{zxy} is negligible respect to σ_{zxxz} or its impact on $V_{\perp}^{2\omega}$ could be cancelled out by the contribution of the non-linear conductivity combined with the ordinary Hall effect, which is also allowed for $\theta = 90^\circ$ with the same $\sin(\beta)$ dependence (for more details, see Supplementary Section 4).

Finally, we studied the microscopic mechanism of the eMChA. For that purpose, we employed a similar analysis as performed for the anomalous Hall effect [42] and the non-linear Hall effect [5], taking into account the peculiarities of the eMChA [20,43]. The procedure relies on how the different physical mechanisms that could cause the observed effect depends on the resistivity of the material. By understanding these dependencies, we can disentangle the mechanisms at play by examining the scaling law between the output voltage, in this case $V_{\perp}^{2\omega}$, and the resistivity of the material, ρ_{xx} :

$$\frac{V_{\perp}^{2\omega}}{(I^\omega)^2} = \gamma + \delta \rho_{xx} + \xi \rho_{xx}^2 \quad (8)$$

where ξ is a resistivity-independent parameter, and γ and δ only depend on the residual resistivity of the material. The intrinsic contribution of the eMChA to $V_{\perp}^{2\omega}$ scales linearly with ρ_{xx} [20]. Therefore, the δ term includes intrinsic and extrinsic contributions, while γ and ξ are purely extrinsic contributions (for more details, see Supplementary Section 5). To explore the eMChA scaling law in our Te device, we modulate the resistivity by varying the sample

temperature [Fig. 1(c)]. Within this temperature range, we recorded $V_{\perp}^{2\omega}$ for the current along x -axis ($\theta = 90^\circ$) as a function of the β -angle at $B = 9$ T and $\alpha = 0^\circ$ [Fig. 4(c)]. Hence, we can now represent $V_{\perp}^{2\omega}$ as a function of temperature [inset in Fig. 4(c)] and, thus, as a function of the resistivity [Fig. 4(d)]. By fitting the experimental data to Eq. (8), we discern that the quadratic term dominates and has opposite sign to the linear term, demonstrating that an extrinsic mechanism coming from dynamic sources dominates the eMChA in Te (see Supplementary Section 5). We performed the same analysis for the longitudinal eMChA with the current along the z -axis ($\theta = 0^\circ$), obtaining the same conclusions [Fig. S4, Table S2]. Therefore, we have proposed a scaling law for eMChA, which successfully identified the dominant microscopic mechanism in our Te devices. This methodology paves the way for similar analyses to uncover the microscopic mechanisms behind eMChA in a wide range of non-centrosymmetric systems.

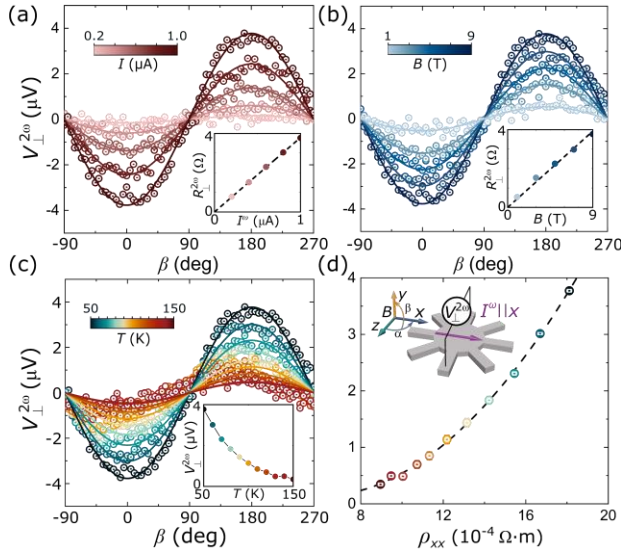


FIG 4. Current-, field- and temperature-dependence of the eMChA in Te. (a), (b), (c) Second-harmonic transverse voltage ($V_{\perp}^{2\omega}$) when current is along the x -axis ($\theta = 90^\circ$) as a function of β -angle for (a) different applied currents ($|I^\omega| = 0.2, 0.4, 0.6, 0.8,$ and $1 \mu\text{A}$) at $B = 9$ T and $T = 50$ K, (b) different external magnetic fields ($B = 1, 3, 5, 7, 9$ T) at $T = 50$ K and $|I^\omega| = 1 \mu\text{A}$, and (c) different temperatures ($T = 50, 60, 70, 80, 90, 100, 110, 120, 130, 140,$ and 150 K) at $B = 9$ T and $|I^\omega| = 1 \mu\text{A}$. (d) Second-harmonic transverse voltage ($V_{\perp}^{2\omega}$) when current is along the x -axis ($\theta = 90^\circ$), obtained from the fittings in panel (c) to Eq. (7), as a function of the resistivity along the x -axis (ρ_{xx}). The dashed line is a fit to Eq. (8). Insets: (a) Current and (b) magnetic field dependence of $R_{\perp}^{2\omega} = V_{\perp}^{2\omega}/I^\omega$, (c) Temperature dependence of $V_{\perp}^{2\omega}$. The values have been obtained from the fittings in panels (a), (b), and (c) to Eq. (7). (d) Sketch of the measurement configurations.

To conclude, we have employed a crystal symmetry analysis of Te electronic transport. At the first order, we have disentangled and quantified the resistivity, magnetoresistance and Hall components. At the second order, we have studied in detail the non-linear transport in response to an external magnetic field, i.e. eMChA. The longitudinal component is allowed when currents and magnetic fields are parallel, demonstrating experimentally the angular momentum texture of Te. The transverse resistance component, as the longitudinal counterpart, scales bilinearly with current and magnetic field, illustrating that both components are different manifestations of the same effect. Finally, we propose a scaling law for eMChA and we apply it to our results in Te, revealing that it is governed by extrinsic mechanisms from dynamic sources.

Acknowledgements

This work is supported by the Spanish MICIU/AEI/10.13039/501100011033 and by ERDF/EU (Projects No. PID2021-122511OB-I00, No. PID2021-128760NB-I00, No. PID2021-129035NB-I00, and “Maria de Maeztu” Units of Excellent Programme No. CEX2020-001038-M). It is also supported by MICIU and by the European Union NextGenerationEU/PRTR-C17.11, as well as by IKUR Strategy under the collaboration agreement between Donostia International Physics Center and CIC nanoGUNE on behalf of the Department of Education of the Basque Government. M. S.-R. acknowledges support from La Caixa Foundation (No. 100010434) with code LCF/BQ/DR21/11880030. B. M.-G. and M. G. thank support from the “Ramón y Cajal” Programme by the Spanish MICIU/AEI and European Union NextGenerationEU/PRTR (Grants No. RYC2021-034836-I and No. RYC2021-031705-I). A. F. acknowledges the support of the UNIVERSIDAD DEL PAIS VASCO as distinguished researcher.

References

- [1] T. Ideue and Y. Iwasa, *Symmetry Breaking and Nonlinear Electric Transport in van Der Waals Nanostructures*, *Annu. Rev. Condens. Matter Phys.* **12**, 201 (2021).
- [2] Z. Z. Du, H.-Z. Lu, and X. C. Xie, *Nonlinear Hall Effects*, *Nat. Rev. Phys.* **3**, 744 (2021).
- [3] Q. Ma et al., *Observation of the Nonlinear Hall Effect under Time-Reversal-Symmetric Conditions*, *Nature* **565**, 337 (2019).

- [4] K. Kang, T. Li, E. Sohn, J. Shan, and K. F. Mak, *Nonlinear Anomalous Hall Effect in Few-Layer WTe₂*, Nat. Mater. **18**, 324 (2019).
- [5] Z. Z. Du, C. M. Wang, S. Li, H. Z. Lu, and X. C. Xie, *Disorder-Induced Nonlinear Hall Effect with Time-Reversal Symmetry*, Nat. Commun. **10**, 3047 (2019).
- [6] Z. Z. Du, C. M. Wang, H. P. Sun, H. Z. Lu, and X. C. Xie, *Quantum Theory of the Nonlinear Hall Effect*, Nat. Commun. **12**, 1 (2021).
- [7] J. Xiao et al., *Berry Curvature Memory through Electrically Driven Stacking Transitions*, Nat. Phys. **16**, 1028 (2020).
- [8] T. Nishijima, T. Watanabe, H. Sekiguchi, Y. Ando, E. Shigematsu, R. Ohshima, S. Kuroda, and M. Shiraishi, *Ferrocic Berry Curvature Dipole in a Topological Crystalline Insulator at Room Temperature*, Nano Lett. **23**, 2247 (2023).
- [9] A. Gao et al., *Quantum Metric Nonlinear Hall Effect in a Topological Antiferromagnetic Heterostructure*, Science **381**, 181 (2023).
- [10] N. Wang et al., *Quantum-Metric-Induced Nonlinear Transport in a Topological Antiferromagnet*, Nature **621**, 487 (2023).
- [11] H. Isobe, S. Y. Xu, and L. Fu, *High-Frequency Rectification via Chiral Bloch Electrons*, Sci. Adv. **6**, 13 (2020).
- [12] D. Kumar, C.-H. Hsu, R. Sharma, T.-R. Chang, P. Yu, J. Wang, E. Goki, G. Liang, and H. Yang, *Room-Temperature Nonlinear Hall Effect and Wireless Radiofrequency Rectification in Weyl Semimetal TaIrTe₄*, Nat. Nanotechnol. **16**, 421 (2021).
- [13] M. Suárez-Rodríguez, B. Martín-García, W. Skowroński, K. Staszek, F. Calavalle, A. Fert, M. Gobbi, F. Casanova, and L.E. Hueso, *Microscale Chiral Rectennas for Energy Harvesting*, Adv. Mater. [10.1002/adma.202400729](https://doi.org/10.1002/adma.202400729) (2024).
- [14] X. F. Lu, C. P. Zhang, N. Wang, D. Zhao, X. Zhou, W. Gao, X. H. Chen, K. T. Law, and K. P. Loh, *Nonlinear Transport and Radio Frequency Rectification in BiTeBr at Room Temperature*, Nat. Commun. **15**, 1 (2024).
- [15] P. He, G. K. W. Koon, H. Isobe, J. Y. Tan, J. Hu, A. H. C. Neto, L. Fu, and H. Yang, *Graphene Moiré Superlattices with Giant Quantum Nonlinearity of Chiral Bloch Electrons*, Nat. Nanotechnol. **17**, 378 (2022).
- [16] M. Suárez-Rodríguez et al., *Odd Nonlinear Conductivity under Spatial Inversion in Chiral Tellurium*, Phys. Rev. Lett. **132**, 046303 (2024).
- [17] A. Tiwari et al., *Giant c-axis Nonlinear Anomalous Hall Effect in T_d-MoTe₂ and WTe₂*, Nat. Commun. **20249** (2021).
- [18] F. Calavalle et al., *Gate-Tuneable and Chirality-Dependent Charge-to-Spin Conversion in Tellurium Nanowires*, Nat. Mater. **21**, 526 (2022).
- [19] G. L. J. A. Rikken and N. Avarvari, *Strong Electrical Magnetochiral Anisotropy in Tellurium*, Phys. Rev. B **99**, 245153 (2019).
- [20] X. Liu, I. Souza, and S. S. Tsirkin, *Electrical Magnetochiral Anisotropy in Trigonal Tellurium from First Principles*, (2023).
- [21] P. He, S. S. L. Zhang, D. Zhu, Y. Liu, Y. Wang, J. Yu, G. Vignale, and H. Yang, *Bilinear Magnetolectric Resistance as a Probe of Three-Dimensional Spin Texture in Topological Surface States*, Nat. Phys. **14**, 495 (2018).
- [22] D. C. Vaz, F. Trier, A. Dyrdał, A. Johansson, K. Garcia, A. Barthélémy, I. Mertig, J. Barnaś, A. Fert, and M. Bibes, *Determining the Rashba Parameter from the Bilinear Magnetoresistance Response in a Two-Dimensional Electron Gas*, Phys. Rev. Mater. **4**, 071001 (2020).
- [23] P. He, S. S. L. Zhang, D. Zhu, S. Shi, O. G. Heinonen, G. Vignale, and H. Yang, *Nonlinear Planar Hall Effect*, Phys. Rev. Lett. **123**, 1 (2019).
- [24] C. Niu, G. Qiu, Y. Wang, P. Tan, M. Wang, J. Jian, H. Wang, W. Wu, and P. D. Ye, *Tunable Chirality-Dependent Nonlinear Electrical Responses in 2D Tellurium*, Nano Lett. **23**, 8445 (2023).
- [25] S. H. Yang, R. Naaman, Y. Paltiel, and S. S. P. Parkin, *Chiral Spintronics*, Nat. Rev. Phys. **3**, 328 (2021).
- [26] R. Naaman, Y. Paltiel, and D. H. Waldeck, *Chiral Molecules and the Electron Spin*, Nat. Rev. Chem. **3**, 250 (2019).
- [27] M. Sakano et al., *Radial Spin Texture in Elemental Tellurium with Chiral Crystal Structure*, Phys. Rev. Lett. **124**, 136404 (2020).
- [28] Y. Wang et al., *Field-Effect Transistors Made from Solution-Grown Two-Dimensional Tellurene*, Nat. Electron. **1**, 228 (2018).
- [29] Y. Du, G. Qiu, Y. Wang, M. Si, X. Xu, W. Wu, and P. D. Ye, *One-Dimensional van Der Waals Material Tellurium: Raman Spectroscopy under Strain and Magneto-Transport*, Nano Lett. **17**, 3965 (2017).
- [30] N. Zhang et al., *Magnetotransport Signatures of Weyl Physics and Discrete Scale Invariance in the*

- Elemental Semiconductor Tellurium*, Proc. Natl. Acad. Sci. U. S. A. **117**, 11337 (2020).
- [31] M. Hirayama, R. Okugawa, S. Ishibashi, S. Murakami, and T. Miyake, *Weyl Node and Spin Texture in Trigonal Tellurium and Selenium*, Phys. Rev. Lett. **114**, 206401 (2015).
- [32] J. Chen et al., *Topological Phase Change Transistors Based on Tellurium Weyl Semiconductor*, Sci. Adv. **8**, 3837 (2022).
- [33] S. V. Gallego, J. Etxebarria, L. Elcoro, E. S. Tasci, and J. M. Perez-Mato, *Automatic Calculation of Symmetry-Adapted Tensors in Magnetic and Non-Magnetic Materials: A New Tool of the Bilbao Crystallographic Server*, Acta. Cryst. **75**, 438 (2019).
- [34] J. Xiong, S. K. Kushwaha, T. Liang, J. W. Krizan, M. Hirschberger, W. Wang, R. J. Cava, and N. P. Ong, *Evidence for the Chiral Anomaly in the Dirac Semimetal Na_3Bi* , Science **350**, 413 (2015).
- [35] A. V. Andreev and B. Z. Spivak, *Longitudinal Negative Magnetoresistance and Magnetotransport Phenomena in Conventional and Topological Conductors*, Phys. Rev. Lett. **120**, 026601 (2018).
- [36] Y. Gao, S. A. Yang, and Q. Niu, *Intrinsic Relative Magnetoconductivity of Nonmagnetic Metals*, Phys. Rev. B **95**, 165135 (2017).
- [37] X. Dai, Z. Z. Du, and H. Z. Lu, *Negative Magnetoresistance without Chiral Anomaly in Topological Insulators*, Phys. Rev. Lett. **119**, 166601 (2017).
- [38] H. K. Pal, *Quantum Contribution to Magnetotransport in Weak Magnetic Fields and Negative Longitudinal Magnetoresistance*, Phys. Rev. B **105**, 075419 (2022).
- [39] S. S. Tsirkin and I. Souza, *On the Separation of Hall and Ohmic Nonlinear Responses*, SciPost Phys. Core **5**, 039 (2022).
- [40] J. Kim and Y. Otani, *Orbital Angular Momentum for Spintronics*, J. Magn. Mater. **563**, 169974 (2022).
- [41] T. Yoda, T. Yokoyama and Y. S. Murakami, *Current-induced Orbital and Spin Magnetizations in Crystals with Helical Structure*, Sci. Rep. **5**, 12024 (2015).
- [42] D. Hou, G. Su, Y. Tian, X. Jin, S. A. Yang, and Q. Niu, *Multivariable Scaling for the Anomalous Hall Effect*, Phys. Rev. Lett. **114**, 217203 (2015).
- [43] A. Dyrdał, J. Barnaś, and A. Fert, *Spin-Momentum-Locking Inhomogeneities as a Source of Bilinear Magnetoresistance in Topological Insulators*, Phys. Rev. Lett. **124**, 046802 (2020).

Supplemental material for:

Symmetry Origin and Microscopic Mechanism of Electrical Magnetochiral Anisotropy in Tellurium

Manuel Suárez-Rodríguez, Beatriz Martín-García, Francesco Calavalle, Stepan S. Tsirkin, Ivo Souza, Fernando De Juan, Albert Fert, Marco Gobbi, Luis E. Hueso, and Félix Casanova.

Contents

Supplementary Section 1. Methods	2
Supplementary Section 2. First-order electronic transport of Tellurium	3
Supplementary Section 3. Second-order electronic transport of Tellurium	9
Supplementary Section 4. How a combination of non-linear conductivity and ordinary Hall can give a contribution that mimics eMChA	12
Supplementary Section 5. Scaling law of eMChA	14

Supplementary Section 1. Methods

I. Chemical Synthesis of Te flakes.-As in our previous paper [16], we synthesized the Te flakes by chemically reducing sodium tellurite (Na_2TeO_3 , 99%) in presence of hydrazine (N_2H_4) in a basic aqueous medium at high temperature. We dissolved at room temperature Na_2TeO_3 (104 mg) and polyvinylpyrrolidone (average M_w 29000-PVP 29, 92.1 mg) in 33 mL of type I water by magnetic stirring. Then, NH_4OH solution (3.65 mL, 25% w in water) and hydrazine hydrate (1.94 mL, 80%, w/w%) were added while stirring. The mixture was transferred to an autoclave that was sealed and heated at 180 °C for 23 h. We purified the resulting material by successive centrifuge-assisted precipitation (10000 rpm-1h, Avanti J-26 XPI centrifuge) and redispersion with type I water. Finally, the Te flakes were redispersed in a dimethylformamide (DMF, $\geq 99.8\%$) and CHCl_3 ($\geq 99.8\%$) mixture (1.3:1 v/v) to be used in the sample fabrication. All the reagents were purchased from Sigma Aldrich and used as received without any further purification.

II. Sample fabrication.-Te flakes were redispersed in a dimethylformamide/ CHCl_3 mixture (1.3:1 v/v) to be used for the drop-casting of solution droplets at the type I-water/air interface in a homemade Langmuir trough. After the evaporation of the solvent, Te flakes floating on the water surface were picked up (Langmuir-Schaefer technique) with Si/ SiO_2 substrates (Si doped n+, 5 x 5 mm, 300 nm thermal oxide). Isolated flakes with suitable dimensions were selected with an optical microscope, without knowing a priori the handedness of the flakes. The flake shape and the contacts were defined through electron-beam lithography performed on a poly(methylmethacrylate)-A4/poly(methylmethacrylate)-A2 double layer. The patterning of the flakes was performed by reactive ion etching (Ar gas, 50 W RF power, 5 x 2 min), and Pt was deposited by sputtering for the electrical contacts. Te has a very anisotropic electrical resistivity and, therefore, the patterning is needed to properly control the current directionality.

III. Electrical measurements.-The devices were wire-bonded to a sample holder and installed in a physical property measurement system (by Quantum Design) for transport measurements with a temperature range of 2-400 K and maximum magnetic field of 9 T. We used a Keithley 6221 to apply a.c. current with a frequency of 31 Hz (ranging from 200 nA to 1 μA) and the longitudinal and transverse voltage drops were measured at the fundamental and the second-harmonic frequencies with a dual channel NF LI5660 lock-in amplifier.

In order to obtain reliable MR, Hall, and eMChA parameters from the angle-dependent measurements, it is crucial to remove any undesired contribution from unavoidable sample tilting (at 9 T even a tiny angle can give a significant contribution). In the first-harmonic transverse experiments, a tilt between the sample and the holder entangles the contributions from ordinary Hall and planar Hall effects. Therefore, to address this issue: (1) in the α -dependence experiments, we measure at positive and negative magnetic fields and calculate the average signal to remove the contribution of the ordinary Hall effect caused by the tilting (which gives a finite, but not constant, β angle) and obtain the clean planar Hall effect signal, and (2) in the β -dependence experiments, we also measure at positive and negative magnetic fields, but in this case, we calculate the half-difference signal to remove the contribution of the planar Hall effect caused by the tilting (which gives a finite, but not constant, α angle) and obtain the ordinary Hall effect signal. By this process, the two effects are disentangled. In the second-harmonic experiments, Te shows a non-linear conductivity at zero-order in B . Hence, to remove the contribution of the non-linear conductivity and to focus on the study of eMChA, we measure at positive and negative magnetic fields and calculate the half-difference signal. This procedure removes the non-linear conductivity contribution, which is at zero-order in B , and leaves the eMChA contribution, which is at first-order in B , unaffected.

Supplementary Section 2. First-order electronic transport of Tellurium

Electrical resistance

The first-order electric field E_i^ω in response to a current j_j^ω in the absence of external magnetic fields can be expressed through the material's resistivity tensor ρ_{ij} as $E_i^\omega = \rho_{ij}j_j^\omega$. For Te with $P3_121$ or $P3_221$ space group symmetry, the resistivity tensor (considering the electric field and the current in the $x - z$ plane) has 2 non-zero elements::

$$\rho_{ij}^{Te} = \begin{pmatrix} \rho_{xx} & 0 \\ 0 & \rho_{zz} \end{pmatrix} \quad (S1)$$

Therefore, the electric field along x - and z -axis in response to a current j_j^ω can be written as:

$$E_x^\omega = \rho_{xx}j_x^\omega \quad (S2)$$

$$E_z^\omega = \rho_{zz}j_z^\omega \quad (S3)$$

For a rotating current in the plane $x - z$, $j_i^\omega = j^\omega(\sin(\theta), 0, \cos(\theta))$:

$$E_x^\omega = \rho_{xx}j^\omega \sin(\theta) \quad (S4)$$

$$E_z^\omega = \rho_{zz}j^\omega \cos(\theta) \quad (S5)$$

Separating in longitudinal and transverse components:

$$E_{\parallel}^\omega = j^\omega[\rho_{xx}\sin^2(\theta) + \rho_{zz}\cos^2(\theta)] \quad (S6)$$

$$E_{\perp}^\omega = j^\omega[\rho_{xx} - \rho_{zz}]\sin(\theta)\cos(\theta) \quad (S7)$$

Now, using: $E_{\parallel}^\omega = V_{\parallel}^\omega/L_{\parallel}$, $E_{\perp}^\omega = V_{\perp}^\omega/L_{\perp}$ and $j^\omega = I^\omega/A$, where L_{\parallel} and L_{\perp} corresponds to the distance between parallel and transverse contacts and A to the cross section, we can rewrite Eqs. (S6) and (S7) in terms of the parameters that we directly measure in our experiments:

$$V_{\parallel}^\omega = \frac{L_{\parallel}}{A}I^\omega[\rho_{xx}\sin^2(\theta) + \rho_{zz}\cos^2(\theta)] \quad (S8)$$

$$V_{\perp}^\omega = \frac{L_{\perp}}{A}I^\omega[\rho_{xx} - \rho_{zz}]\sin(\theta)\cos(\theta) \quad (S9)$$

Magneto-resistance

The first-order electric field E_i^ω in response to a current j_j^ω and a magnetic field $B_{k,l}$ can be expressed through the material's magnetoresistance tensor T_{ijkl} as $E_i^\omega = T_{ijkl}j_j^\omega B_k B_l$. For Te with $P3_121$ or $P3_221$ space group symmetry, the magnetoresistance tensor (considering the electric field and the current in the $x - z$ plane and the magnetic field in all directions) has 9 non-zero elements [33]:

$$T_{ijkl}^{Te} = \begin{pmatrix} T_{xxxx} & T_{xxyy} & T_{xxzz} & T_{xxyz} & 0 & 0 \\ T_{zzxx} & T_{zzyy} & T_{zzzz} & 0 & 0 & 0 \\ 0 & 0 & 0 & 0 & T_{zxzx} & T_{zxzy} \end{pmatrix} \quad (S10)$$

Therefore, the electric field along x - and z -axis in response to a current j_j^ω and a magnetic field $B_{k,l}$ can be written as:

$$E_x^\omega = T_{xxxx}j_x^\omega B_x^2 + T_{xxyy}j_x^\omega B_y^2 + T_{xxzz}j_x^\omega B_z^2 + T_{xxyz}j_x^\omega B_y B_z + T_{zxzx}j_x^\omega B_x B_z + T_{zxzy}j_x^\omega B_x B_y \quad (S11)$$

$$E_z^\omega = T_{zzxx}j_z^\omega B_x^2 + T_{zzyy}j_z^\omega B_y^2 + T_{zzzz}j_z^\omega B_z^2 + T_{zxzx}j_z^\omega B_x B_z + T_{zxzy}j_z^\omega B_x B_y \quad (S12)$$

Thus, for a rotating magnetic field in all directions, $B_i = B(\sin(\alpha)\cos(\beta), \sin(\beta), \cos(\alpha)\cos(\beta))$:

$$E_x^\omega = T_{xxxx}j_x^\omega B^2 \sin^2(\alpha)\cos^2(\beta) + T_{xxyy}j_x^\omega B^2 \sin^2(\beta) + T_{xxzz}j_x^\omega B^2 \cos^2(\alpha)\cos^2(\beta) + T_{xxyz}j_x^\omega B^2 \cos(\alpha)\sin(\beta)\cos(\beta) + T_{zxzx}j_z^\omega B^2 \sin(\alpha)\cos(\alpha)\cos^2(\beta) + T_{zxzy}j_z^\omega B^2 \sin(\alpha)\sin(\beta)\cos(\beta) \quad (S13)$$

$$E_z^\omega = T_{zzxx}j_z^\omega B^2 \sin^2(\alpha)\cos^2(\beta) + T_{zzyy}j_z^\omega B^2 \sin^2(\beta) + T_{zzzz}j_z^\omega B^2 \cos^2(\alpha)\cos^2(\beta) + T_{zxzx}j_x^\omega B^2 \sin(\alpha)\cos(\alpha)\cos^2(\beta) + T_{xzyy}j_x^\omega B^2 \sin(\alpha)\sin(\beta)\cos(\beta) \quad (S14)$$

If now we consider a rotating current in the plane $x - z$, $j_i^\omega = j^\omega(\sin(\theta), 0, \cos(\theta))$, we obtain:

$$E_x^\omega = 2j^\omega \cos(\theta) B^2 [T_{xxzx} \sin(\alpha)\cos(\alpha)\cos^2(\beta) + T_{xzyy} \sin(\alpha)\sin(\beta)\cos(\beta)] + j^\omega \sin(\theta) B^2 [T_{xxxx} \sin^2(\alpha)\cos^2(\beta) + T_{xxyy} \sin^2(\beta) + T_{xxzz} \cos^2(\alpha)\cos^2(\beta) + T_{xxyz} \cos(\alpha)\sin(\beta)\cos(\beta)] \quad (S15)$$

$$E_z^\omega = 2j^\omega \sin(\theta) B^2 [T_{xxzx} \sin(\alpha)\cos(\alpha)\cos^2(\beta) + T_{xzyy} \sin(\alpha)\sin(\beta)\cos(\beta)] + j^\omega \cos(\theta) B^2 [T_{zzxx} \sin^2(\alpha)\cos^2(\beta) + T_{zzyy} \sin^2(\beta) + T_{zzzz} \cos^2(\alpha)\cos^2(\beta)] \quad (S16)$$

Finally, separating in longitudinal and transverse components:

$$E_{\parallel}^\omega = 2j^\omega \sin(\theta)\cos(\theta) B^2 [T_{xxzx} \sin(\alpha)\cos(\alpha)\cos^2(\beta) + T_{xzyy} \sin(\alpha)\sin(\beta)\cos(\beta)] + j^\omega \cos^2(\theta) B^2 [T_{zzxx} \sin^2(\alpha)\cos^2(\beta) + T_{zzyy} \sin^2(\beta) + T_{zzzz} \cos^2(\alpha)\cos^2(\beta)] + j^\omega \sin^2(\theta) B^2 [T_{xxxx} \sin^2(\alpha)\cos^2(\beta) + T_{xxyy} \sin^2(\beta) + T_{xxzz} \cos^2(\alpha)\cos^2(\beta) + T_{xxyz} \cos(\alpha)\sin(\beta)\cos(\beta)] \quad (S17)$$

$$E_{\perp}^\omega = 2j^\omega [\cos^2(\theta) - \sin^2(\theta)] B^2 [T_{xxzx} \sin(\alpha)\cos(\alpha)\cos^2(\beta) + T_{xzyy} \sin(\alpha)\sin(\beta)\cos(\beta)] + j^\omega \sin(\theta)\cos(\theta) B^2 [T_{xxxx} \sin^2(\alpha)\cos^2(\beta) + T_{xxyy} \sin^2(\beta) + T_{xxzz} \cos^2(\alpha)\cos^2(\beta) + T_{xxyz} \cos(\alpha)\sin(\beta)\cos(\beta) - T_{zzxx} \sin^2(\alpha)\cos^2(\beta) - T_{zzyy} \sin^2(\beta) - T_{zzzz} \cos^2(\alpha)\cos^2(\beta)] \quad (S18)$$

Hall contribution

Now, we will include also the Hall contribution. The first-order Hall response to a current j_j^ω and a magnetic field B_k^ω can be expressed through the material's Hall tensor R_{ijk} as $E_i^\omega = R_{ijk} j_j^\omega B_k$. For Te with $P3_121$ or $P3_221$ space group symmetry, the Hall tensor (considering the electric field and the current in the $x - z$ plane and the magnetic field in all directions) has 2 non-zero elements [33]:

$$R_{ijk}^{Te} = \begin{pmatrix} 0 & 0 & 0 \\ 0 & R_{xzy} & 0 \\ 0 & -R_{xzy} & 0 \\ 0 & 0 & 0 \end{pmatrix} \quad (S19)$$

Therefore, the Hall contribution of the electric field along x - and z -axis can we written as:

$$E_x = R_{xzy} j_z B_y \quad (S20)$$

$$E_z = -R_{xzy} j_x B_y \quad (S21)$$

Thus, for a rotating magnetic field in all directions $B_i = B(\sin(\alpha)\cos(\beta), \sin(\beta), \cos(\alpha)\cos(\beta))$:

$$E_x^\omega = R_{xzy} j_z^\omega B \sin(\beta) \quad (S22)$$

$$E_z^\omega = -R_{xzy} j_x^\omega B \sin(\beta) \quad (S23)$$

If now we consider a rotating current in the plane $x - z$, $j_i^\omega = j^\omega(\sin(\theta), 0, \cos(\theta))$:

$$E_x^\omega = R_{xzy}j^\omega \cos(\theta) B \sin(\beta) \quad (\text{S24})$$

$$E_z^\omega = -R_{xzy}j^\omega \sin(\theta) B \sin(\beta) \quad (\text{S25})$$

Finally, separating in longitudinal and transverse components:

$$E_{\parallel}^\omega = 0 \quad (\text{S26})$$

$$E_{\perp}^\omega = R_{xzy}j^\omega [\sin^2(\theta) + \cos^2(\theta)] B \sin(\beta) \quad (\text{S27})$$

As expected, the Hall contribution is purely transverse.

All first-order contributions

If we take into account all first-order contributions: electrical resistance, magnetoresistance and Hall, we obtain:

$$\begin{aligned} E_{\parallel}^\omega &= j^\omega [\rho_{xx} \sin^2(\theta) + \rho_{zz} \cos^2(\theta)] + \\ &2j^\omega \sin(\theta) \cos(\theta) [T_{xzxz} B^2 \sin(\alpha) \cos(\alpha) \cos^2(\beta) + T_{xzxy} \sin(\alpha) \sin(\beta) \cos(\beta)] + \\ &j^\omega \cos^2(\theta) B^2 [T_{zzxx} \sin^2(\alpha) \cos^2(\beta) + T_{zzyy} \sin^2(\beta) + T_{zzzz} \cos^2(\alpha) \cos^2(\beta)] + \\ &j^\omega \sin^2(\theta) B^2 [T_{xxxx} \sin^2(\alpha) \cos^2(\beta) + T_{xxyy} \sin^2(\beta) + T_{xxzz} \cos^2(\alpha) \cos^2(\beta) + T_{xxyz} \cos(\alpha) \sin(\beta) \cos(\beta)] \end{aligned} \quad (\text{S28})$$

$$\begin{aligned} E_{\perp}^\omega &= j^\omega [\rho_{xx} - \rho_{zz}] \sin(\theta) \cos(\theta) + \\ &2j^\omega [\cos^2(\theta) - \sin^2(\theta)] B^2 [T_{xzxz} \sin(\alpha) \cos(\alpha) \cos^2(\beta) + T_{xzxy} \sin(\alpha) \sin(\beta) \cos(\beta)] \\ &+ j^\omega \sin(\theta) \cos(\theta) B^2 [T_{xxxx} \sin^2(\alpha) \cos^2(\beta) + T_{xxyy} \sin^2(\beta) + T_{xxzz} \cos^2(\alpha) \cos^2(\beta) + \\ &T_{xxyz} \cos(\alpha) \sin(\beta) \cos(\beta) - T_{zzxx} \sin^2(\alpha) \cos^2(\beta) - T_{zzyy} \sin^2(\beta) - T_{zzzz} \cos^2(\alpha) \cos^2(\beta)] + \\ &R_{xzy} j^\omega [\sin^2(\theta) + \cos^2(\theta)] B \sin(\beta) \end{aligned} \quad (\text{S29})$$

Now, using: $E_{\parallel}^\omega = V_{\parallel}^\omega / L_{\parallel}$, $E_{\perp}^\omega = V_{\perp}^\omega / L_{\perp}$ and $j^\omega = I^\omega / A$, we can rewrite the expressions (S28) and (S29) in terms of the parameters that we directly measure in our experiments:

$$\begin{aligned} V_{\parallel}^\omega &= \frac{L_{\parallel}}{A} I^\omega [\rho_{xx} \sin^2(\theta) + \rho_{zz} \cos^2(\theta)] + \\ &2 \frac{L_{\parallel}}{A} I^\omega \sin(\theta) \cos(\theta) B^2 [T_{xzxz} \sin(\alpha) \cos(\alpha) \cos^2(\beta) + T_{xzxy} \sin(\alpha) \sin(\beta) \cos(\beta)] + \\ &\frac{L_{\parallel}}{A} I^\omega \cos^2(\theta) B^2 [T_{zzxx} \sin^2(\alpha) \cos^2(\beta) + T_{zzyy} \sin^2(\beta) + T_{zzzz} \cos^2(\alpha) \cos^2(\beta)] + \\ &\frac{L_{\parallel}}{A} I^\omega \sin^2(\theta) B^2 [T_{xxxx} \sin^2(\alpha) \cos^2(\beta) + T_{xxyy} \sin^2(\beta) + T_{xxzz} \cos^2(\alpha) \cos^2(\beta) + T_{xxyz} \cos(\alpha) \sin(\beta) \cos(\beta)] \end{aligned} \quad (\text{S30})$$

$$\begin{aligned} V_{\perp}^\omega &= \frac{L_{\perp}}{A} I^\omega [\rho_{xx} - \rho_{zz}] \sin(\theta) \cos(\theta) + \\ &2 \frac{L_{\perp}}{A} I^\omega [\cos^2(\theta) - \sin^2(\theta)] B^2 [T_{xzxz} \sin(\alpha) \cos(\alpha) \cos^2(\beta) + T_{xzxy} \sin(\alpha) \sin(\beta) \cos(\beta)] + \\ &\frac{L_{\perp}}{A} I^\omega \sin(\theta) \cos(\theta) B^2 [T_{xxxx} \sin^2(\alpha) \cos^2(\beta) + T_{xxyy} \sin^2(\beta) + T_{xxzz} \cos^2(\alpha) \cos^2(\beta) + \\ &T_{xxyz} \cos(\alpha) \sin(\beta) \cos(\beta) - T_{zzxx} \sin^2(\alpha) \cos^2(\beta) - T_{zzyy} \sin^2(\beta) - T_{zzzz} \cos^2(\alpha) \cos^2(\beta)] + \\ &R_{xzy} \frac{L_{\perp}}{A} I^\omega [\sin^2(\theta) + \cos^2(\theta)] B \sin(\beta) \end{aligned} \quad (\text{S31})$$

To simplify the analysis, we will study the magnetoresistance and Hall contributions for the particular cases of current j^ω applied along z -axis ($\theta = 0^\circ$):

$$V_{\parallel}^\omega = \frac{L_{\parallel}}{A} I^\omega \rho_{zz} + \frac{L_{\parallel}}{A} I^\omega B^2 [T_{zzxx} \sin^2(\alpha) \cos^2(\beta) + T_{zzyy} \sin^2(\beta) + T_{zzzz} \cos^2(\alpha) \cos^2(\beta)] \quad (\text{S32})$$

$$V_{\perp}^\omega = 2 \frac{L_{\perp}}{A} I^\omega B^2 [T_{xzzz} \sin(\alpha) \cos(\alpha) \cos^2(\beta) + T_{xzyy} \sin(\alpha) \sin(\beta) \cos(\beta)] + R_{xzy} \frac{L_{\perp}}{A} I^\omega B \sin(\beta) \quad (\text{S33})$$

and along the x -axis ($\theta = 90^\circ$):

$$V_{\parallel}^\omega = \frac{L_{\parallel}}{A} I^\omega \rho_{xx} + \frac{L_{\parallel}}{A} I^\omega B^2 [T_{xxxx} \sin^2(\alpha) \cos^2(\beta) + T_{xxyy} \sin^2(\beta) + T_{xxzz} \cos^2(\alpha) \cos^2(\beta) + T_{xxyz} \cos(\alpha) \sin(\beta) \cos(\beta)] \quad (\text{S34})$$

$$V_{\perp}^\omega = -2 \frac{L_{\perp}}{A} I^\omega B^2 [T_{xzzz} \sin(\alpha) \cos(\alpha) \cos^2(\beta) + T_{xzyy} \sin(\alpha) \sin(\beta) \cos(\beta)] + R_{xzy} \frac{L_{\perp}}{A} I^\omega B \sin(\beta) \quad (\text{S35})$$

Moreover, to isolate the different components, we will consider 2 different rotating planes for the magnetic field: (1) α -angle dependence with $\beta = 0^\circ$, and (2) β -angle dependence with $\alpha = 0^\circ$. Therefore, we have in total 4 cases: (a) α -angle dependence with $\beta = 0^\circ$ and $\theta = 0^\circ$:

$$V_{\parallel}^\omega = \frac{L_{\parallel}}{A} I^\omega \rho_{zz} + \frac{L_{\parallel}}{A} I^\omega B^2 [T_{zzxx} \sin^2(\alpha) + T_{zzzz} \cos^2(\alpha)] \quad (\text{S36})$$

$$V_{\perp}^\omega = 2 \frac{L_{\perp}}{A} I^\omega B^2 T_{xzzz} \sin(\alpha) \cos(\alpha) \quad (\text{S37})$$

(b) β -angle dependence with $\alpha = 0^\circ$ and $\theta = 0^\circ$:

$$V_{\parallel}^\omega = \frac{L_{\parallel}}{A} I^\omega \rho_{zz} + \frac{L_{\parallel}}{A} I^\omega B^2 [T_{zzyy} \sin^2(\beta) + T_{zzzz} \cos^2(\beta)] \quad (\text{S38})$$

$$V_{\perp}^\omega = R_{xzy} \frac{L_{\perp}}{A} I^\omega B \sin(\beta) \quad (\text{S39})$$

(c) α -angle dependence with $\beta = 0^\circ$ and $\theta = 90^\circ$:

$$V_{\parallel}^\omega = \frac{L_{\parallel}}{A} I^\omega \rho_{xx} + \frac{L_{\parallel}}{A} I^\omega B^2 [T_{xxxx} \sin^2(\alpha) + T_{xxzz} \cos^2(\alpha)] \quad (\text{S40})$$

$$V_{\perp}^\omega = -2 \frac{L_{\perp}}{A} I^\omega B^2 T_{xzzz} \sin(\alpha) \cos(\alpha) \quad (\text{S41})$$

(d) β -angle dependence with $\alpha = 0^\circ$ and $\theta = 90^\circ$:

$$V_{\parallel}^\omega = \frac{L_{\parallel}}{A} I^\omega \rho_{xx} + \frac{L_{\parallel}}{A} I^\omega B^2 [T_{xxyy} \sin^2(\beta) + T_{xxzz} \cos^2(\beta) + T_{xxyz} \sin(\beta) \cos(\beta)] \quad (\text{S42})$$

$$V_{\perp}^\omega = R_{xzy} \frac{L_{\perp}}{A} I^\omega B \sin(\beta) \quad (\text{S43})$$

Therefore, from symmetry considerations, we have obtained the equations which describe the first-order electronic transport in Te.

Experimental results

We start exploring the zero-field resistivity components. For that purpose, we measured the longitudinal, V_{\parallel}^ω [Fig. S1(a)] and transverse, V_{\perp}^ω [Fig. S1(b)] first-harmonic voltage as a function of the

θ -angle, between the current I^ω and the chiral z -axis, in the absence of external magnetic fields. We represent the slope of each curve in front of the θ -angle [Fig. 1(e)]. As observed, equations (S8) and (S9) perfectly fit the experimental data, demonstrating a precise control of the current directionality in our devices.

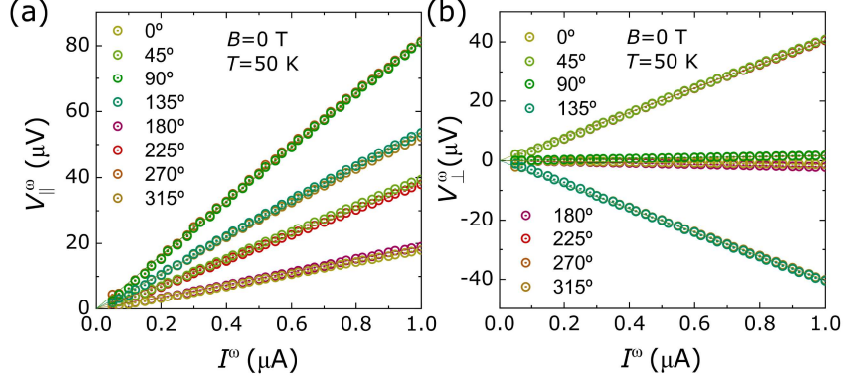


FIG. S1. Zero-field anisotropic resistivity. First-harmonic longitudinal V_{\parallel}^{ω} (a) and transverse V_{\perp}^{ω} (b) voltage as a function of I^{ω} at 50 K for different θ angles. The solid lines are linear fits to the experimental data.

Next, we measured the longitudinal magnetoresistance $MR = \frac{R_{\parallel}^{\omega}(B=9T) - R_{\parallel}^{\omega}(B=0T)}{R_{\parallel}^{\omega}(B=0T)}$ for both $\theta = 0^\circ$ [Fig. 2(a)] and $\theta = 90^\circ$ [Fig. 2(b)], as a function of (i) α -angle with $\beta = 0^\circ$ (black curves) and (ii) β -angle with $\alpha = 0^\circ$ (red curves). From equations (S36), (S38), (S40), and (S42) we can obtain directly the equations to fit our experimental data:

$$\theta = 0^\circ, \beta = 0^\circ, \alpha\text{-dep} \rightarrow MR = \frac{1}{\rho_{zz}} B^2 [T_{zzxx} \sin^2(\alpha) + T_{zzzz} \cos^2(\alpha)] \quad (\text{S44})$$

$$\theta = 0^\circ, \alpha = 0^\circ, \beta\text{-dep} \rightarrow MR = \frac{1}{\rho_{zz}} B^2 [T_{zzyy} \sin^2(\beta) + T_{zzzz} \cos^2(\beta)] \quad (\text{S45})$$

$$\theta = 90^\circ, \beta = 0^\circ, \alpha\text{-dep} \rightarrow MR = \frac{1}{\rho_{xx}} B^2 [T_{xxxx} \sin^2(\alpha) + T_{xxzz} \cos^2(\alpha)] \quad (\text{S46})$$

$$\theta = 90^\circ, \alpha = 0^\circ, \beta\text{-dep} \rightarrow MR = \frac{1}{\rho_{xx}} B^2 [T_{xxyy} \sin^2(\beta) + T_{xxzz} \cos^2(\beta) + T_{xxyz} \sin(\beta) \cos(\beta)] \quad (\text{S47})$$

As we can observe, these equations perfectly capture the experimental response [Fig. 2(a),(b)]. To further study the longitudinal magnetoresistance, we also measured the MR as a function of the magnetic field when applied along x -, y -, and z -axis, both for $\theta = 0^\circ$ [Fig. S2(a)] and $\theta = 90^\circ$ [Fig. S2(b)]. Independently on the current direction, the material shows negative MR when B is aligned with the z -axis. The MR curves do not follow a parabolic dependence with B . However, they are even with respect to B , as expected. The later, differentiate a transverse signal arising from the magnetoresistance from a true Hall effect, which is odd with B [39] (for more details, see Hall contribution section).

We also study the temperature dependence of the MR between 10 K and 200 K. We focus on the MR for $\theta = 0^\circ$, when B is applied along the z - as well as the x -axis. As we can observe in Fig. S2(c), when B is applied along the z -axis, the MR magnitude decreases with increasing the temperature, but still negative between 0 and 9 T. In contrast, when B is applied along the x -axis (Fig. S2(d)), we observe significant changes with temperature. At 10 K, it is negative until approximately 4 T

and then becomes flat. At 50 K, it is negative until approximately 3 T and then becomes positive and parabolic. Finally, for 100 K and higher temperatures, the MR is positive and parabolic for the whole magnetic field range.

Now, we focus on the transverse response. For that purpose, we measured the transverse first-harmonic resistance $R_{\perp}^{\omega} = \frac{V_{\perp}^{\omega}}{I^{\omega}}$ for both $\theta = 0^{\circ}$ [Fig. 2(c)] and $\theta = 90^{\circ}$ [Fig. 2(d)], as a function of (i) α -angle with $\beta = 0^{\circ}$ (black curves) and (ii) β -angle with $\alpha = 0^{\circ}$ (red curves). From equations (S37), (S39), (S41), and (S43) we can obtain the equation to fit our experimental data:

$$\theta = 0^{\circ}, \beta = 0^{\circ}, \alpha\text{-dep} \rightarrow R_{\perp}^{\omega} = 2 \frac{L_{\perp}}{A} B^2 T_{xxzx} \sin(\alpha) \cos(\alpha) \quad (\text{S48})$$

$$\theta = 0^{\circ}, \alpha = 0^{\circ}, \beta\text{-dep} \rightarrow R_{\perp}^{\omega} = R_{xzy} \frac{L_{\perp}}{A} B \sin(\beta) \quad (\text{S49})$$

$$\theta = 90^{\circ}, \beta = 0^{\circ}, \alpha\text{-dep} \rightarrow R_{\perp}^{\omega} = -2 \frac{L_{\perp}}{A} B^2 T_{xxzx} \sin(\alpha) \cos(\alpha) \quad (\text{S50})$$

$$\theta = 90^{\circ}, \alpha = 0^{\circ}, \beta\text{-dep} \rightarrow R_{\perp}^{\omega} = R_{xzy} \frac{L_{\perp}}{A} B \sin(\beta) \quad (\text{S51})$$

We highlight that the component T_{xxzx} describes what is usually called planar Hall effect. However, it is even with B and it comes directly from the MR tensor, so it is not a true Hall effect. Moreover, the amplitude of the Planar Hall effect [Fig. 2(c),(d)] (black curves) is much lower than the one of the longitudinal MR [Fig. 2(a),(b)]. In the measurements of planar Hall effect in ferromagnets, the amplitude is linked to the amplitude of the longitudinal anisotropic MR , but here it is not, T_{xxzx} is independent to T_{xxxx} , T_{xxzz} , T_{zzxx} , and T_{zzzz} . To further study the Hall component R_{xzy} , we also measured R_{\perp}^{ω} as a function of B_y for $\theta = 0^{\circ}$ [Fig. S2(e)] and $\theta = 90^{\circ}$ [Fig. 2(f)]. From the positive sign, we identify that the transport is dominated by holes; and from the magnitude ($R_{\perp}^{\omega} = B_y/t n_p e$), we obtain the carrier density at 50 K: $n_p \approx 6.5 \times 10^{17} \text{cm}^{-3}$. Finally, we summarize in Table S1 the values of resistivity, MR and Hall components obtained from the fittings of the experimental data.

TABLE. S1. Dimensions, zero-field resistivity, MR and Hall components at 50 K and 9 T.

Dimensions	t (μm)	0.11
	w (μm)	0.79
	A (μm^2)	0.087
	L_{\parallel} (μm)	2.95
	L_{\perp} (μm)	4.27
Resistivity	ρ_{xx} (Ωm)	$1.81 \cdot 10^{-3}$
	ρ_{zz} (Ωm)	$4.09 \cdot 10^{-4}$
MR components	T_{xxxx} ($\text{VmA}^{-1}\text{T}^{-2}$)	$(1.01 \pm 0.19) \cdot 10^{-7}$
	T_{xxyy} ($\text{VmA}^{-1}\text{T}^{-2}$)	$(4.94 \pm 0.22) \cdot 10^{-7}$
	T_{xxzz} ($\text{VmA}^{-1}\text{T}^{-2}$)	$(-1.178 \pm 0.021) \cdot 10^{-6}$
	T_{xxyz} ($\text{VmA}^{-1}\text{T}^{-2}$)	≈ 0
	T_{zzxx} ($\text{VmA}^{-1}\text{T}^{-2}$)	$(2.77 \pm 0.17) \cdot 10^{-8}$
	T_{zzyy} ($\text{VmA}^{-1}\text{T}^{-2}$)	$(1.360 \pm 0.022) \cdot 10^{-7}$
	T_{zzzz} ($\text{VmA}^{-1}\text{T}^{-2}$)	$(-1.658 \pm 0.017) \cdot 10^{-7}$
	T_{zxzx} ($\text{VmA}^{-1}\text{T}^{-2}$)	$(2.74 \pm 0.19) \cdot 10^{-9}$
Hall component	R_{xzy} ($\text{VmA}^{-1}\text{T}^{-1}$)	$(1.754 \pm 0.013) \cdot 10^{-6}$

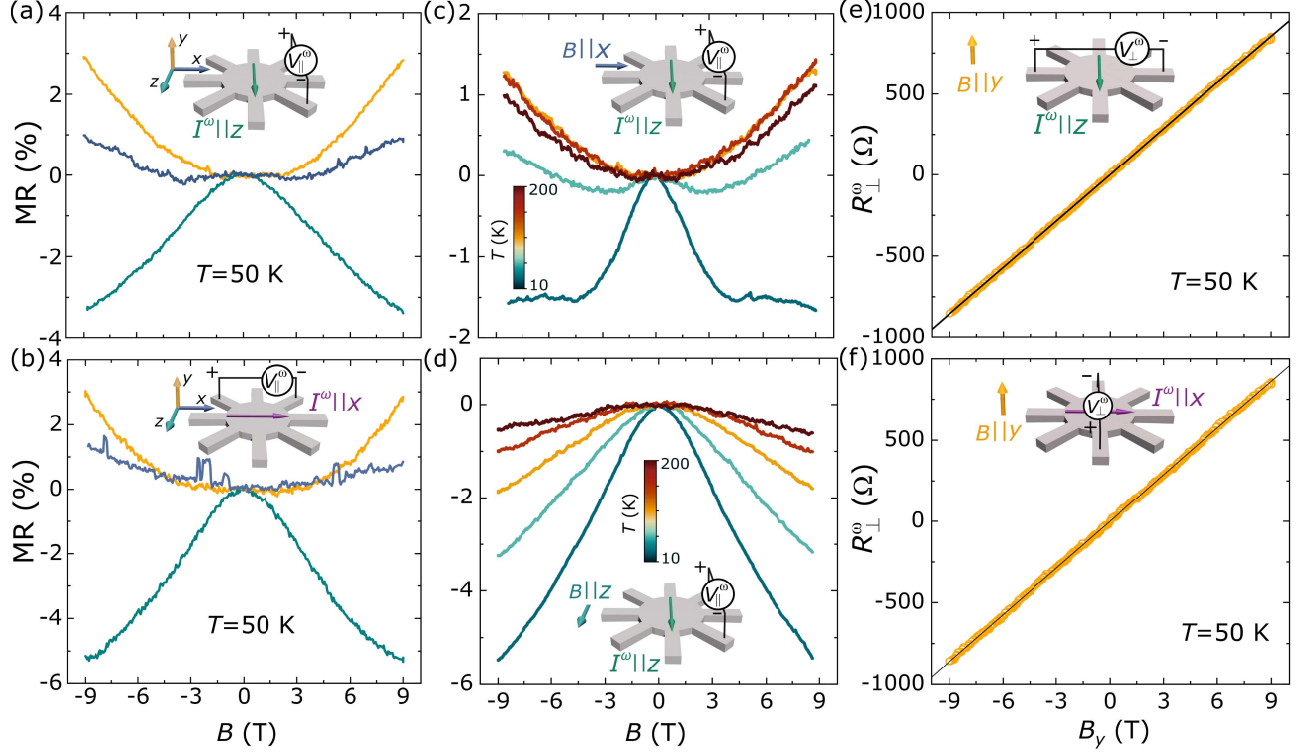


FIG. S2. Additional data of first-order electronic transport on Te. (a), (b) Longitudinal MR as a function of B when applied along x -, y -, and z -axis, for (a) $\theta = 0^\circ$ and (b) $\theta = 90^\circ$ at 50 K. (c), (d), Temperature dependence of longitudinal MR for $\theta = 0^\circ$ as a function of B when applied along the (c) x -axis and (d) z -axis. (e), (f), R_{\perp}^{ω} as a function of B_y for (e) $\theta = 0^\circ$ and (f) $\theta = 90^\circ$ at 50 K.

Supplementary Section 3. Second-order electronic transport of Tellurium

The second-order nonlinear current density $j_i^{2\omega}$ in response to an electric field $E_{j,k}^{\omega}$ and magnetic field B_l can be expressed through the material eMChA conductivity tensor σ_{ijkl} as $j_i^{2\omega} = \sigma_{ijkl} E_j^{\omega} E_k^{\omega} B_l$. For Te with $P3_121$ or $P3_221$ point group symmetry, the eMChA tensor (considering the electric field and the current density in the $x-z$ plane and the magnetic field in all directions) has 8 independent non-zero elements [33]:

$$\sigma_{ijkl} = \begin{pmatrix} \sigma_{xxxx} & \sigma_{xzzx} & 0 \\ 0 & 0 & \sigma_{xxzy} \\ 0 & 0 & \sigma_{xxzz} \\ 0 & 0 & \sigma_{zxxx} \\ 0 & \sigma_{zxy} & 0 \\ \sigma_{zxzx} & \sigma_{zzzz} & 0 \end{pmatrix} \quad (\text{S52})$$

For an in-plane electric field $E_k^{\omega} = (E_x^{\omega}, 0, E_z^{\omega})$, the second-order current density $j_i^{2\omega}$ is given by:

$$\begin{pmatrix} j_x^{2\omega} \\ j_z^{2\omega} \end{pmatrix} = \begin{pmatrix} \sigma_{xxxx} E_x^{\omega} B_x + \sigma_{xzzx} E_z^{\omega} B_x + 2\sigma_{xxzy} E_x E_z B_y + 2\sigma_{xxzz} E_x E_z B_y \\ 2\sigma_{zxzx} E_x E_z B_x + \sigma_{zxy} E_x^2 B_y + \sigma_{zxxx} E_x^2 B_z + \sigma_{zzzz} E_z^2 B_z \end{pmatrix} \quad (\text{S53})$$

In our experiments, we apply current and measure voltages. Therefore, we have to swap from conductivities to resistivities. Considering the electrical and eMChA conductivities, the current response is given by:

$$j_i = \sigma_{ij}^0 E_j^\omega + \sigma_{ijkl} E_j^\omega E_k^\omega B_l \quad (\text{S54})$$

We define the analog coefficients in resistivity as:

$$E_i = \rho_{ij} j_j^\omega + \rho_{ijkl} j_j^\omega j_k^\omega B_l \quad (\text{S55})$$

Plugging Eq. (S55) back into Eq. (S54) and equating order by order, we can obtain the eMChA resistivity ρ_{ijkl} :

$$\sigma_{ij}^0 \rho_{jklm} j_k^\omega j_l^\omega B_m + \sigma_{ijkl} \rho_{jkm} j_m^\omega \rho_{kn} j_n^\omega B_l = 0 \quad (\text{S56})$$

which gives after some relabeling:

$$\rho_{abcd} = -\sigma_{ijmd} \rho_{ia} \rho_{jb} \rho_{mc} \quad (\text{S57})$$

Therefore, now we can write the second-order electric field $E^{2\omega}$ as a function of σ_{ijkl} :

$$\begin{pmatrix} E_x^{2\omega} \\ E_z^{2\omega} \end{pmatrix} = - \begin{pmatrix} \rho_{xx}^3 \sigma_{xxxx} (j_x^\omega)^2 B_x + \rho_{xx} \rho_{zz}^2 \sigma_{zzxx} (j_z^\omega)^2 B_x + 2\rho_{xx}^2 \rho_{zz} \sigma_{xxzy} j_x^\omega j_z^\omega B_y + 2\rho_{xx}^2 \rho_{zz} \sigma_{xxzz} j_x^\omega j_z^\omega B_y \\ 2\rho_{xx} \rho_{zz}^2 \sigma_{zzxx} j_x^\omega j_z^\omega B_x + \rho_{xx}^2 \rho_{zz} \sigma_{zxy} (j_x^\omega)^2 B_y + \rho_{xx}^2 \rho_{zz} \sigma_{zxxz} (j_x^\omega)^2 B_z + \rho_{zz}^3 \sigma_{zzzz} (j_z^\omega)^2 B_z \end{pmatrix} \quad (\text{S58})$$

For an in-plane current $j_i^\omega = j^\omega (\sin(\theta), 0, \cos(\theta))$ of amplitude j^ω and angle θ measured from the chiral axis (z -axis):

$$\begin{aligned} \frac{E_x^{2\omega}}{(j^\omega)^2} &= -\rho_{xx}^3 \sigma_{xxxx} \sin^2(\theta) B_x - \rho_{xx} \rho_{zz}^2 \sigma_{zzxx} \cos^2(\theta) B_x \\ &- 2\rho_{xx}^2 \rho_{zz} \sigma_{xxzy} \sin(\theta) \cos(\theta) B_y - 2\rho_{xx}^2 \rho_{zz} \sigma_{xxzz} \sin(\theta) \cos(\theta) B_z \end{aligned} \quad (\text{S59})$$

$$\begin{aligned} \frac{E_z^{2\omega}}{(j^\omega)^2} &= 2\rho_{xx} \rho_{zz}^2 \sigma_{zzxx} \sin(\theta) \cos(\theta) B_x - \rho_{xx}^2 \rho_{zz} \sigma_{zxy} \sin^2(\theta) B_y \\ &- \rho_{xx}^2 \rho_{zz} \sigma_{zxxz} \sin^2(\theta) B_z - \rho_{zz}^3 \sigma_{zzzz} \cos^2(\theta) B_z \end{aligned} \quad (\text{S60})$$

Separating parallel and transverse components:

$$\begin{aligned} \frac{E_{\parallel}^{2\omega}}{(j^\omega)^2} &= -\rho_{xx}^3 \sigma_{xxxx} \sin^3(\theta) B_x - \rho_{zz}^3 \sigma_{zzzz} \cos^3(\theta) B_z - [\rho_{xx}^2 \rho_{zz} \sigma_{zxy} + 2\rho_{xx}^2 \rho_{zz} \sigma_{xxzy}] \sin^2(\theta) \cos(\theta) B_y \\ &- [\rho_{xx}^2 \rho_{zz} \sigma_{zxxz} + 2\rho_{xx}^2 \rho_{zz} \sigma_{xxzz}] \sin^2(\theta) \cos(\theta) B_z - [\rho_{xx} \rho_{zz}^2 \sigma_{zzxx} + 2\rho_{xx} \rho_{zz}^2 \sigma_{zxxz}] \sin(\theta) \cos^2(\theta) B_x \end{aligned} \quad (\text{S61})$$

$$\begin{aligned} \frac{E_{\perp}^{2\omega}}{(j^\omega)^2} &= \rho_{xx}^2 \rho_{zz} \sigma_{zzxx} \sin^3(\theta) B_z - \rho_{xx} \rho_{zz}^2 \sigma_{zzxx} \cos^3(\theta) B_x + [-\rho_{xx}^3 \sigma_{xxxx} + 2\rho_{xx} \rho_{zz}^2 \sigma_{zxxz}] \sin^2(\theta) \cos(\theta) B_x \\ &+ [\rho_{zz}^3 \sigma_{zzzz} - 2\rho_{xx}^2 \rho_{zz} \sigma_{xxzz}] \sin(\theta) \cos^2(\theta) B_z - 2\rho_{xx}^2 \rho_{zz} \sigma_{xxzy} \sin(\theta) \cos^2(\theta) B_y + \rho_{xx}^2 \rho_{zz} \sigma_{zxy} \sin^3(\theta) B_y \end{aligned} \quad (\text{S62})$$

For a rotating magnetic field: $\mathbf{B} = B(\sin(\alpha)\cos(\beta), \sin(\beta), \cos(\alpha)\cos(\beta))$, we obtain:

$$\begin{aligned} \frac{E_{\parallel}^{2\omega}}{(j\omega)^2} = & -\rho_{xx}^3\sigma_{xxxx}\sin^3(\theta)B\sin(\alpha)\cos(\beta) - \rho_{zz}^3\sigma_{zzzz}\cos^3(\theta)B\cos(\alpha)\cos(\beta) - [\rho_{xx}^2\rho_{zz}\sigma_{xxxy} + \\ & 2\rho_{xx}^2\rho_{zz}\sigma_{xxzy}]\sin^2(\theta)\cos(\theta)B\sin(\beta) - [\rho_{xx}^2\rho_{zz}\sigma_{xxxz} + 2\rho_{xx}^2\rho_{zz}\sigma_{xxzz}]\sin^2(\theta)\cos(\theta)B\sin(\alpha)\cos(\beta) - \\ & [\rho_{xx}\rho_{zz}^2\sigma_{zzzx} + 2\rho_{xx}\rho_{zz}^2\sigma_{zzxz}]\sin(\theta)\cos^2(\theta)B\sin(\alpha)\cos(\beta) \end{aligned} \quad (\text{S63})$$

$$\begin{aligned} \frac{E_{\perp}^{2\omega}}{(j\omega)^2} = & \rho_{xx}^2\rho_{zz}\sigma_{zzxz}\sin^3(\theta)B\cos(\alpha)\cos(\beta) - \rho_{xx}\rho_{zz}^2\sigma_{zzzx}\cos^3(\theta)B\sin(\alpha)\cos(\beta) - [\rho_{xx}^3\sigma_{xxxx} + \\ & 2\rho_{xx}\rho_{zz}^2\sigma_{zzxz}]\sin^2(\theta)\cos(\theta)B\sin(\alpha)\cos(\beta) + [\rho_{zz}^3\sigma_{zzzz} - 2\rho_{xx}^2\rho_{zz}\sigma_{xxzz}]\sin(\theta)\cos^2(\theta)B\cos(\alpha)\cos(\beta) - \\ & 2\rho_{xx}^2\rho_{zz}\sigma_{xxzy}\sin(\theta)\cos^2(\theta)B\sin(\beta) + \rho_{xx}^2\rho_{zz}\sigma_{xxxy}\sin^3(\theta)B\sin(\beta) \end{aligned} \quad (\text{S64})$$

As in previous sections, we study the particular cases of j_i^ω applied along x - ($\theta = 90^\circ$) and z -axis ($\theta = 0^\circ$). We obtain for $E_{\parallel}^{2\omega}$:

$$\theta = 0^\circ \rightarrow \frac{E_{\parallel}^{2\omega}}{(j\omega)^2} = -\rho_{zz}^3\sigma_{zzzz}B\cos(\alpha)\cos(\beta) \quad (\text{S65})$$

$$\theta = 90^\circ \rightarrow \frac{E_{\parallel}^{2\omega}}{(j\omega)^2} = -\rho_{xx}^3\sigma_{xxxx}B\sin(\alpha)\cos(\beta) \quad (\text{S66})$$

And for $E_{\perp}^{2\omega}$:

$$\theta = 0^\circ \rightarrow \frac{E_{\perp}^{2\omega}}{(j\omega)^2} = -\rho_{xx}\rho_{zz}^2\sigma_{zzxz}B\sin(\alpha)\cos(\beta) \quad (\text{S67})$$

$$\theta = 90^\circ \rightarrow \frac{E_{\perp}^{2\omega}}{(j\omega)^2} = -\rho_{xx}^2\rho_{zz}\sigma_{zzxz}B\cos(\alpha)\cos(\beta) \quad (\text{S68})$$

Finally, using: $E_{\parallel}^{2\omega} = V_{\parallel}^{2\omega}/L_{\parallel}$, $E_{\perp}^{2\omega} = V_{\perp}^{2\omega}/L_{\perp}$ and $j^\omega = I^\omega/A$, we can rewrite Eqs. (S63) and (S64) in terms of the parameters that we directly measure in our experiments. We obtain for $V_{\parallel}^{2\omega}$:

$$\theta = 0^\circ \rightarrow \frac{V_{\parallel}^{2\omega}}{(I^\omega)^2} = -\frac{L_{\parallel}}{A^2}\rho_{zz}^3\sigma_{zzzz}B\cos(\alpha)\cos(\beta) \quad (\text{S69})$$

$$\theta = 90^\circ \rightarrow \frac{V_{\parallel}^{2\omega}}{(I^\omega)^2} = -\frac{L_{\parallel}}{A^2}\rho_{xx}^3\sigma_{xxxx}B\sin(\alpha)\cos(\beta) \quad (\text{S70})$$

And for $V_{\perp}^{2\omega}$:

$$\theta = 0^\circ \rightarrow \frac{V_{\perp}^{2\omega}}{(I^\omega)^2} = -\frac{L_{\perp}}{A^2}\rho_{xx}\rho_{zz}^2\sigma_{zzxz}B\sin(\alpha)\cos(\beta) \quad (\text{S71})$$

$$\theta = 90^\circ \rightarrow \frac{V_{\perp}^{2\omega}}{(I^\omega)^2} = -\frac{L_{\perp}}{A^2}\rho_{xx}^2\rho_{zz}\sigma_{zzxz}B\cos(\alpha)\cos(\beta) \quad (\text{S72})$$

Which are equations (4), (5), (6) and (7) in the main text.

We investigate $V_{\parallel}^{2\omega}$ (Fig. 3a) and $V_{\perp}^{2\omega}$ (Fig. 3b) as a function of α -angle at $\beta = 0^\circ$ and $|B|= 9$ T, for current along z -axis ($\theta = 0^\circ$) and x -axis ($\theta = 90^\circ$). As observed, the equations obtained from our symmetry analysis perfectly capture the experimental response.

On the following, we will focus on the transverse eMChA, i.e. non-linear planar Hall effect, at $\theta = 90^\circ$. In the main text, in order to further study this component, we recorded $V_\perp^{2\omega}$ for different currents at $B = 9$ T [Fig. 4(a)] and for different magnetic fields at $|I^\omega| = 1\mu A$ [Fig. 4(b)], as a function of β -angle at $\alpha = 0^\circ$. Here, we also explore the current and field dependence of $V_\perp^{2\omega}$ but rotating B in the α -plane at $\beta = 0^\circ$ [Fig. S3]. As observed, our equations perfectly fit the experimental data both in the α - and β -angle dependence studies (solid lines in Fig. S3 and 4, respectively). We summarize in the main text the values of the eMChA components obtained from the fittings of the experimental data to equations (S65), (S66) and (S68).

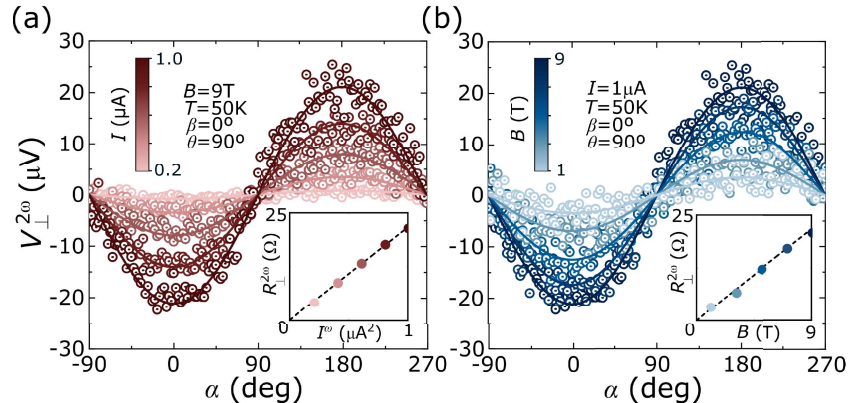


FIG. S3. Non-linear planar Hall effect. (a), (b) Second-harmonic transverse voltage ($V_\perp^{2\omega}$) when current is along the x -axis ($\theta = 90^\circ$) and $\beta = 0^\circ$ as a function of α -angle for (a) different applied currents ($|I^\omega| = 0.2, 0.4, 0.6, 0.8,$ and $1.0 \mu A$) at 9 T and 50 K, (b) different external magnetic fields ($B = 1, 3, 5, 7, 9$ T) at 50 K and $|I^\omega| = 1\mu A$. Insets: (a) Current I^ω , and (b) Magnetic field B dependence of $R_\perp^{2\omega} = V_\perp^{2\omega}/I^\omega$. The values have been obtained from the fittings in the main panels (a) and (b) to Eq. (S72).

Supplementary Section 4. How a combination of non-linear conductivity and ordinary Hall can give a contribution that mimics eMChA

If we also take into account the non-linear conductivity χ_{ijk} [16] and the Hall conductivity σ_{ijk}^H , we realize that more terms, by the combination of different contributions, appear into the resistivity. In general, the full current response is given by:

$$j_i = \sigma_{ij}^0 E_j^\omega + \chi_{ijk} E_j^\omega E_k^\omega + \sigma_{ijk}^H E_j^\omega B_k + \sigma_{ijkl} E_j^\omega E_k^\omega B_l \quad (S73)$$

where we have considered the electrical conductivity σ_{ij}^0 , the non-linear conductivity χ_{ijk} [16], the Hall conductivity σ_{ijk}^H , and the eMChA conductivity σ_{ijkl} . We define the analog coefficients in resistivity as:

$$E_i = \rho_{ij} j_j^\omega + \rho_{ijk}^{(2)} j_j^\omega j_k^\omega + R_{ijk} j_j^\omega B_k + \rho_{ijkl} j_j^\omega j_k^\omega B_l \quad (S74)$$

Plugging Eq. (S74) back into Eq. (S73) and equating order by order, we can relate conductivities to resistivities. At zero-order in B and first-order in E we find $\sigma_{ij}^0 \rho_{jk} = \sigma_{ik}$. To second-order in E , we find:

$$\sigma_{ij}^0 \rho_{jkl}^{(2)} j_k^\omega j_l^\omega + \chi_{ijk} \rho_{jkm} j_m^\omega \rho_{kn} j_n^\omega = 0 \quad (S75)$$

which is equivalent to:

$$\rho_{jkl}^{(2)} j_k^\omega j_l^\omega = -\rho_{pi} \chi_{ijk} \rho_{jm} \rho_{kn} j_m^\omega j_n^\omega \quad (\text{S76})$$

Now, relabeling indices:

$$\rho_{ijk}^{(2)} = -\rho_{il} \chi_{imn} \rho_{mj} \rho_{nk} \quad (\text{S77})$$

To first-order in B and E , we find:

$$\sigma_{ij}^0 R_{jkl} j_k^\omega B_l + \sigma_{ijk}^H \rho_{jm} j_m^\omega B_k = 0 \quad (\text{S78})$$

which gives:

$$R_{jkl} = -\rho_{il} \sigma_{lmk}^H \rho_{mj} \quad (\text{S79})$$

Finally, to second-order in E and first-order in B , we have:

$$\sigma_{ij}^0 \rho_{jklm} j_k^\omega j_l^\omega B_m + \chi_{ijk} (\rho_{jl} j_l^\omega R_{kmn} j_m^\omega B_n + R_{jmn} j_m^\omega B_n \rho_{kl} j_l^\omega) + \sigma_{ijk}^H \rho_{jnm}^{(2)} j_n^\omega j_m^\omega B_k + \sigma_{ijkl} \rho_{jm} j_m^\omega \rho_{kn} j_n^\omega B_l = 0 \quad (\text{S80})$$

which gives after some relabeling:

$$\rho_{abcd} = [(\chi_{ijk} \sigma_{lmd}^H + \chi_{imk} \sigma_{ljd}^H + \chi_{kjm} \sigma_{ild}^H) \rho_{kl} - \sigma_{ijmd}] \rho_{ia} \rho_{jb} \rho_{mc} \quad (\text{S81})$$

To summarize, the relationship between resistivities and conductivities is given by:

$$\rho_{ij} = (\sigma_{ij}^0)^{-1} \quad (\text{S82})$$

$$\rho_{ijk}^{(2)} = -\rho_{il} \chi_{imn} \rho_{mj} \rho_{nk} \quad (\text{S83})$$

$$R_{jkl} = -\rho_{il} \sigma_{lmk}^H \rho_{mj} \quad (\text{S84})$$

$$\rho_{abcd} = [(\chi_{ijk} \sigma_{lmd}^H + \chi_{imk} \sigma_{ljd}^H + \chi_{kjm} \sigma_{ild}^H) \rho_{kl} - \sigma_{ijmd}] \rho_{ia} \rho_{jb} \rho_{mc} \quad (\text{S85})$$

The last term in equation (S85) refers to the eMChA contribution, and the first three terms to the combination of non-linear conductivity and Hall effect. For Te, with $P3_121$ or $P3_221$ space group (twofold axis in the x -direction and chiral axis in z -direction), we have $\rho_{xx} = \rho_{yy}$ and ρ_{zz} for resistivity, $\sigma_{zxy}^H = -\sigma_{zyx}^H$ and σ_{xyz}^H for Hall, and $\chi_{xxx} = -\chi_{xyy} = -\chi_{yxy}$ and $\chi_{xyz} = -\chi_{yzx}$ for non-linear conductivity. Therefore, for our material we obtain:

$$\rho_{zzzz} = -\sigma_{zzzz} \rho_{zz}^3 \quad (\text{S86})$$

$$\rho_{xxxx} = -\sigma_{xxxx} \rho_{xx}^3 \quad (\text{S87})$$

$$\rho_{zxxz} = -\sigma_{zxxz} \rho_{zz} \rho_{xx}^2 \quad (\text{S88})$$

$$\rho_{zxxy} = -\sigma_{zxxy} \rho_{zz} \rho_{xx}^2 + \chi_{xxx} \sigma_{zxy}^H \rho_{xx}^3 \rho_{zz} \quad (\text{S89})$$

$$\rho_{xzzx} = -\sigma_{xzzx} \rho_{xx} \rho_{zz}^2 + 2\chi_{xzy} \sigma_{yzx}^H \rho_{xx} \rho_{zz}^3 \quad (\text{S90})$$

Taking into account all the contributions to $V^{2\omega}$:

$$\theta = 0^\circ \rightarrow \frac{V_{\parallel}^{2\omega}}{(I\omega)^2} = -\frac{L_{\parallel}}{A^2} \rho_{zz}^3 \sigma_{zzzz} B \cos(\alpha) \cos(\beta) \quad (\text{S91})$$

$$\theta = 90^\circ \rightarrow \frac{V_{\parallel}^{2\omega}}{(I\omega)^2} = -\frac{L_{\parallel}}{A^2} \rho_{xx}^3 \sigma_{xxxx} B \sin(\alpha) \cos(\beta) - \frac{L_{\parallel}}{A^2} \rho_{xx}^3 \chi_{xxx} \quad (\text{S92})$$

$$\theta = 0^\circ \rightarrow \frac{V_{\perp}^{2\omega}}{(I\omega)^2} = -\frac{L_{\perp}}{A^2} \rho_{xx} \rho_{zz}^2 \sigma_{xzzx} B \sin(\alpha) \cos(\beta) + 2\frac{L_{\perp}}{A^2} \chi_{xzy} \sigma_{yzx}^H \rho_{yy} \rho_{xx} \rho_{zz}^2 B \sin(\alpha) \cos(\beta) \quad (\text{S93})$$

$$\theta = 90^\circ \rightarrow \frac{V_{\perp}^{2\omega}}{(I\omega)^2} = -\frac{L_{\perp}}{A^2} \rho_{xx} \rho_{zz}^2 \sigma_{xzzx} B \cos(\alpha) \cos(\beta) - \frac{L_{\perp}}{A^2} \rho_{xx} \rho_{zz}^2 \sigma_{zxxy} B \sin(\beta) + \frac{L_{\perp}}{A^2} \chi_{xxx} \sigma_{zxy}^H \rho_{xx}^3 \rho_{zz} B \sin(\beta) \quad (\text{S94})$$

We note that the term $\frac{L_{\parallel}}{A^2}\rho_{xx}^3\chi_{xxx}$ in Eq. (S92) does not contribute to our magnetotransport experiments, because we measure at positive and negative magnetic fields and we calculate the half-difference. Therefore, terms at zero-order in B are removed (for more details, see Supplementary Section 1, *III. Electrical measurements*).

Supplementary Section 5. Scaling law of eMChA

To unveil the microscopic mechanism behind a transport effect it is convenient to study the scaling law of the output voltage with the resistivity of the material. This methodology has been developed for many years and finally polished by Hou *et al.* [42] to study the anomalous Hall effect, and later adapted by Du *et al* [5] to understand the non-linear Hall effect. The scaling law of the non-linear Hall effect proposed by Du *et al* [5] has the following form:

$$\frac{V_{\perp}^{2\omega}}{(I\omega)^2} = C_1\rho_{xx0} + C_2\rho_{xx0}^2 + C_3\rho_{xx0}\rho_{xxT} + C_4\rho_{xxT}^2 \quad (\text{S95})$$

with four scaling parameters:

$$\begin{aligned} C_1 &= C^{sk} \\ C_2 &= C^{in} + C_0^{sj} + C_{00}^{sj} \\ C_3 &= 2C^{in} + C_0^{sj} + C_1^{sj} + C_{01}^{sj} \\ C_4 &= C^{in} + C_1^{sj} + C_{11}^{sj} \end{aligned} \quad (\text{S96})$$

where the disorder-independent coefficients are for the intrinsic (C^{in}), side-jump (C_i^{sj} , C_{ij}^{sj}), and skew-scattering (C^{sk}) contributions, respectively. The indexes i , j refer to different scattering sources. We have considered one static ($i, j = 0$) and one dynamic ($i, j = 1$) source.

Here, we apply the same strategy to study the microscopic mechanism behind the eMChA in Te, taking into account the particularities of this effect. Following Liu *et al.* results [20], the intrinsic contribution of the eMChA scales with τ^2 , being τ the scattering time. Hence, the intrinsic eMChA scales linearly with the resistivity of the material ρ . Therefore, the scaling law of eMChA can be written as:

$$\frac{V_{\perp}^{2\omega}}{(I\omega)^2} = C_1\rho_{xx0} + C_2\rho_{xxT} + C_3\rho_{xx0}^2 + C_4\rho_{xx0}\rho_{xxT} + C_5\rho_{xxT}^2 \quad (\text{S97})$$

with five scaling parameters:

$$\begin{aligned} C_1 &= C^{sk} + C^{in} \\ C_2 &= C^{in} \\ C_3 &= C_0^{sj} + C_{00}^{sj} \\ C_4 &= C_0^{sj} + C_1^{sj} + C_{01}^{sj} \\ C_5 &= C_1^{sj} + C_{11}^{sj} \end{aligned} \quad (\text{S98})$$

We note that the disorder-independent coefficient for the intrinsic contribution (C^{in}) is included in parameters C_1 and C_2 which carry the linear dependence with the resistivity of the material. ρ_{xx0} is the residual resistivity due to static impurities at zero temperature and $\rho_{xxT} = \rho_{xx} - \rho_{xx0}$ is due to dynamic disorder at finite temperature. Hence, we can rewrite the expression in terms of ρ_{xx} , our experimental variable:

$$\frac{V_{\perp}^{2\omega}}{(I\omega)^2} = \gamma + \delta\rho_{xx} + \xi\rho_{xx}^2 \quad (\text{S99})$$

where:

$$\begin{aligned}
\gamma &= (C_1 - C_2)\rho_{xx0} + (C_3 - C_4 + C_5)\rho_{xx0}^2 = C^{sk}\rho_{xx0} + (C_{00}^{sk} - C_{01}^{sk} + C_{11}^{sk})\rho_{xx0}^2 \\
\delta &= (C_4 - 2C_5)\rho_{xx0} + C_2 = C^{in} + (C_0^{sj} + C_{01}^{sk} - C_1^{sj} - 2C_{11}^{sk})\rho_{xx0} \\
\xi &= C_5 = C_1^{sj} + C_{11}^{sk}
\end{aligned} \tag{S100}$$

We note that in our experimentally practical parsing of eMChA, the above definitions have not relied on identification of semiclassical processes such as side-jump scattering or skew scattering from asymmetric contributions to the semiclassical scattering rates [42]. In the full semiclassical theory, we are aware that considering the skew-scattering contribution as the sum of all the contributions arising from the asymmetric scattering rate present in the collision term of the Boltzman transport equation, there is a term which scales with $\rho_i\rho_j/\rho^3$, known as intrinsic skew-scattering [5]. However, we do not categorize this contribution as skew-scattering but rather place it under the umbrella of side-jump (C_i^{sj}), following the approach used in previous works studying the multivariable scaling of transport effects [42].

To explore the eMChA scaling law, we modulate the resistivity by varying the sample temperature [Fig. 1(c)]. In the main text, we investigate the transverse component for $\theta = 90^\circ$. Here, we also include the study of the longitudinal component for $\theta = 0^\circ$. In this configuration, the scaling law can be written as:

$$\frac{V_{\parallel}^{2\omega}}{(I\omega)^2} = \gamma + \delta\rho_{zz} + \xi\rho_{zz}^2 \tag{S101}$$

where:

$$\begin{aligned}
\gamma &= C^{sk}\rho_{zz0} + (C_{00}^{sk} - C_{01}^{sk} + C_{11}^{sk})\rho_{zz0}^2 \\
\delta &= C^{in} + (C_0^{sj} + C_{01}^{sk} - C_1^{sj} - 2C_{11}^{sk})\rho_{zz0} \\
\xi &= C_1^{sj} + C_{11}^{sk}
\end{aligned} \tag{S102}$$

Hence, we record $V_{\parallel}^{2\omega}$ for $\theta = 0^\circ$ as a function of the α -angle at $B = 9$ T and $\beta = 0^\circ$ [Fig. S4(a)]. Now, we can plot $V_{\parallel}^{2\omega}$ as a function of temperature [Fig. S4(b)], and as a function of the resistivity [Fig. S4(c)]. By fitting the experimental results to Eq. (S101), we also unveil that the quadratic term dominates and has opposite sign than the longitudinal term (Table S2). Therefore, we can confirm that both longitudinal and tranverse eMChA in Te are dominated by extrinsic mechanism from dynamic sources. In table S2, we summarize the values of γ , δ and ξ obtained from the fittings of the experimental data to Eqs. (S97) and (S99).

TABLE. S2. γ , δ and ξ values obtained from the fitting of the experimental data.

	γ (VA^{-2})	δ ($\text{A}^{-1}\text{m}^{-1}$)	ξ ($\text{m}^{-2}\text{V}^{-1}$)
Transverse	$-9.6 \pm 2.9 \cdot 10^{-7}$	$2.89 \pm 0.46 \cdot 10^{-3}$	-2.44 ± 0.17
Longitudinal	$1.28 \pm 0.14 \cdot 10^{-5}$	$-8.84 \pm 0.78 \cdot 10^{-2}$	156 ± 11

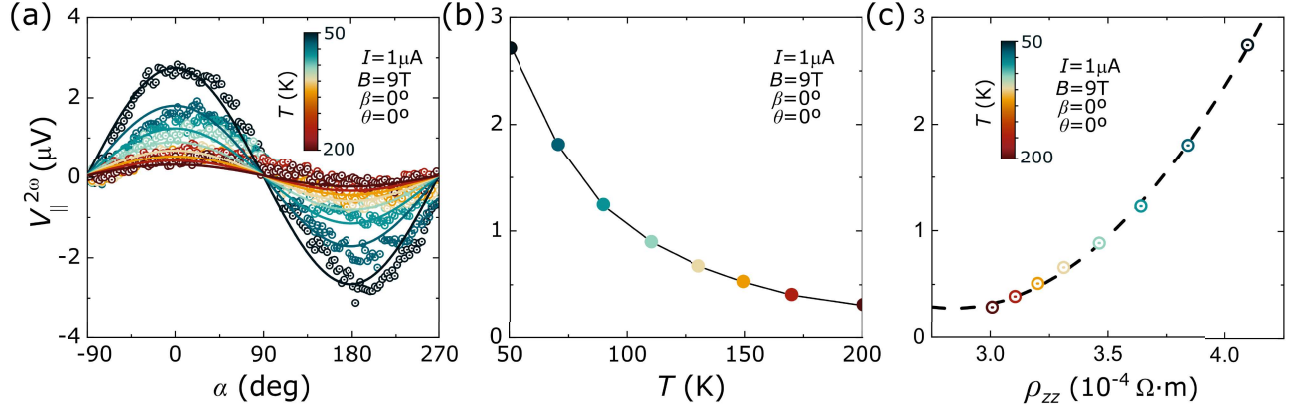


FIG. S4. Scaling law of eMChA. Second-harmonic longitudinal voltage ($V_{\parallel}^{2\omega}$) when current is along the z -axis ($\theta = 0^\circ$) as a function of (a) α -angle for different temperatures ($T = 50, 70, 90, 110, 130, 150, 170$ and 200 K), (b) temperature, and (c) resistivity along the z -axis (ρ_{zz}). The measurements were performed at 9 T, $\beta = 0^\circ$, and $|I^\omega| = 1 \mu\text{A}$.